The Astrophysical Journal, 708:675–697, 2010 January 1 doi:10.1088/0004-637X/708/1/675

LONG-TERM MONITORING OF THE DYNAMICS AND PARTICLE ACCELERATION OF KNOTS IN THE JET OF CENTAURUS A

J. L. Goodger[1], M. J. Hardcastle[1], J. H. Croston[2], R. P. Kraft[3], M. Birkinshaw[3,4], D. A. Evans[5], A. Jordán[3,6], P. E. J. Nulsen[3], G. R. Sivakoff[7], D. M. Worrall[3,4], N. J. Brassington[3], W. R. Forman[3], M. Gilfanov[8], C. Jones[3], S. S. Murray[3], S. Raychaudhury[9], C. L. Sarazin[7], R. Voss[10], and K. A. Woodley[11]

[1] School of Physics, Astronomy & Mathematics, University of Hertfordshire, College Lane, Hatfield AL10 9AB, UK; j.l.goodger@herts.ac.uk, m.j.hardcastle@herts.ac.uk

[2] University of Southampton, University Road, Southampton SO17 1BJ, UK; J.Croston@soton.ac.uk

[3] Harvard-Smithsonian Center for Astrophysics, 60 Garden Street, Cambridge, MA 02138, USA; kraft@head.cfa.harvard.edu, nbrassington@cfa.harvard.edu, wforman@cfa.harvard.edu, cjones@cfa.harvard.edu, ssm@cfa.harvard.edu, pnulsen@cfa.harvard.edu

[4] Department of Physics, University of Bristol, Tyndall Avenue, Bristol BS8 ITL, UK; mark.birkinshaw@bristol.ac.uk, d.m.worrall@bristol.ac.uk

[5] MIT Kavli Institute for Astrophysics and Space Research, 77 Massachusetts Avenue, Cambridge, MA 02139, USA; devans@space.mit.edu

[6] Departamento de Astronomía y Astrofísica, Pontificia Universidad Católica de Chile, 7820436 Macul, Santiago, Chile; ajordan@astro.puc.cl

[7] Department of Astronomy, University of Virginia, P.O. Box 400325, Charlottesville, VA 22904-4325, USA; sarazin@virginia.edu, grs8g@virginia.edu

[8] Max Planck Institute fur Astrophysik Karl-Schwarzschild-Str 1 D-85741 Garching, Germany; gilfanov@MPA-Garching.mpg.de

[9] School of Physics and Astronomy, University of Birmingham, Edgbaston, Birmingham B15 2TT, UK; somak@star.sr.bham.ac.uk

[10] Excellence Cluster Universe Technische Universitt Munchen Boltzmannstr 2 D-85748 Garching, Germany; rvoss@mpe.mpg.de

[11] Department of Physics and Astronomy, McMaster University, Hamilton, ON L8S 4M1, Canada; woodleka@physics.mcmaster.ca

[12] European Southern Observatory, Karl-Schwarzschild-Str. 2 85748 Garching bei München, Germany

Received 2009 September 18; accepted 2009 November 12; published 2009 December 15

ABSTRACT

We present new and archival multi-frequency radio and X-ray data for Centaurus A obtained over almost 20 years at the Very Large Array and with *Chandra*, with which we measure the X-ray and radio spectral indices of jet knots, flux density variations in the jet knots, polarization variations, and proper motions. We compare the observed properties with current knot formation models and particle acceleration mechanisms. We rule out impulsive particle acceleration as a formation mechanism for all of the knots as we detect the same population of knots in all of the observations, and we find no evidence of extreme variability in the X-ray knots. We find that the most likely mechanism for all the stationary knots is a collision resulting in a local shock followed by a steady state of prolonged, stable particle acceleration, and X-ray synchrotron emission. In this scenario, the X-ray-only knots have radio counterparts that are too faint to be detected, while the radio-only knots are due to weak shocks where no particles are accelerated to X-ray emitting energies. Although the base knots are prime candidates for reconfinement shocks, the presence of a moving knot in this vicinity and the fact that there are two base knots are hard to explain in this model. We detect apparent motion in three knots; however, their velocities and locations provide no conclusive evidence for or against a faster moving "spine" within the jet. The radio-only knots, both stationary and moving, may be due to compression of the fluid.

Key words: galaxies: active – galaxies: individual (Centaurus A, NGC 5128) – galaxies: jets – X-rays: galaxies

1. INTRODUCTION

It is generally agreed that the observed emission from Fanaroff–Riley class I (FR I; Fanaroff & Riley 1974) radio jets is due to the synchrotron process at all wavelengths, with similar jet structure observed from the radio through the optical into the X-ray (e.g., Hardcastle et al. 2002; Harris & Krawczynski 2002). The jets of FR I radio galaxies are thought to decelerate as they move away from the core, entraining material and expanding into a plume of diffuse matter (e.g., Bicknell 1984). One of the most significant implications of the synchrotron emission model is reflected in the characteristic loss timescales: in a stable environment, the X-ray-emitting electrons have lifetimes of the order of tens of years, tracing regions of current, in situ particle acceleration, while the radio-emitting electrons last for hundreds of thousands of years, showing the history of particle acceleration in the jet.

In order to investigate these regions of particle acceleration, we need data with sensitivity and resolution sufficient to detect jet substructure on spatial scales comparable to the synchrotron loss scales. This prompts us to look to the two closest bright FR I radio jets: M87 and Centaurus A (NGC 5128, hereafter Cen A). Both of these jets have been detected in multiple frequencies from the radio to the X-ray (e.g., Feigelson et al. 1981; Kraft et al. 2002; Hardcastle et al. 2003, 2006; Harris & Krawczynski 2002). The proximity of these radio galaxies, 16.7 Mpc and 3.7 Mpc, respectively (Blakeslee et al. 2009; Mei et al. 2007; Ferrarese et al. 2007), makes them unique jet laboratories with spatial scales of 77 pc and 17 pc per arcsec, respectively. The details revealed in the structure of these jets have been the focus of many recent studies (e.g., Biretta et al. 1999; Hardcastle et al. 2003; Kataoka et al. 2006; Cheung et al. 2007). Within the smooth surface brightness observed in both of these jets are clumps of bright material—the knots—embedded in diffuse material, all emitting via synchrotron emission. The precise mechanisms causing the particle acceleration responsible for the diffuse structure and the knots are still unknown.

The most surprising result of recent observations of these two systems was the radio-to-X-ray synchrotron flare of HST-1 in M87. In 2002, the X-ray flux of HST-1 increased by a factor of 2 in only 116 days (Harris et al. 2003), implying a change within an emitting volume with a characteristic size less than 0.1 pc for a stationary source (much less than the size of HST-1, ∼3 pc). The X-ray brightness then faded in the following months only to flare again, peaking in 2005. At its brightest, this flare was higher than its 2001 level by a factor of ∼50. The UV and radio

light curves were found to vary in step with the X-ray up to this peak (Perlman et al. 2003; Harris et al. 2006), but the subsequent decrease appeared to drop off faster in the X-ray than in either the optical or the UV, which drop off in step (Harris et al. 2009). In addition to this spectral variability, it was established with the *Hubble Space Telescope* (*HST*) and the NRAO Very Long Baseline Array (VLBA) that some of the knots in M87 move superluminally, including subregions of the HST-1 knot (Biretta et al. 1999; Cheung et al. 2007). Together, this suggests that we are observing synchrotron losses in addition to either beaming or compression/rarefaction of the fluid.

Cen A is a factor of 4.5 closer than M87, so we can resolve more details in the complicated fine structure of the jet. The originally identified features, named A–G by Feigelson et al. (1981), have since been resolved into at least 40 individual knots (Kraft et al. 2002; Hardcastle et al. 2003) with additional emission from diffuse material. Some of the diffuse emission has been described as downstream "tails" of emission from the knots (Hardcastle et al. 2003) or as evidence for limb brightening of the jet (Kraft et al. 2000). In 2003, Hardcastle et al. presented 8.4 GHz radio observations from the NRAO Very Large Array (VLA) of Cen A. That work used archival data from 1991 and new observations from 2002 to study the jet knots and investigated the offsets and relationships between the radio knots and their X-ray counterparts and vice versa. They found that only some of the radio knots appeared to have X-ray counterparts, leaving many as "radio-only" knots and "X-ray-only" knots. They also considered the temporal changes in the radio knots, specifically their proper motions, finding that some of the radio knots were moving. These moving knots had comparatively little X-ray emission suggesting that high-energy particle acceleration is less efficient in these regions than in the jet as a whole.

Some of the current models explaining the presence of knots within the generally smooth diffuse material of the jet include compressions in the fluid flow, collisions with obstacles in the galaxy causing local shocks, reconfinement of the jet or some other jet-wide process, and magnetic reconnection. Hardcastle et al. (2003) ruled out simple compression of the fluid as a mechanism for producing X-ray bright, radio faint compact knots in favor of in situ particle acceleration associated with local shocks; however, compression could still play a part in the other knots. They concluded that the most likely model to describe the majority of these knots is an interaction between the jet fluid and an obstacle such as a molecular cloud or a high-mass-loss star. By exploring the temporal behavior of the X-ray and radio emission, we can understand the evolution of the knots and constrain the various models of particle acceleration used to describe the jet features.

In this work, we use *Chandra* and VLA data spread over almost 20 years to measure the X-ray and radio spectral indices knots, flux density variations, polarization variations, and the proper motions of the jet knots in Cen A. Our aims are to detect variability in the radio and X-ray properties of the knots, either extreme variability similar to that of HST-1 in M87 or more subtle changes, and to compare these properties. which will allow us to constrain the knot formation processes at work in the jet of Cen A. The details of our radio and X-ray data reduction are discussed in Section 2. In Section 3, we discuss the details of our analysis methods and the global results for the knot population, highlighting particularly interesting features. In Section 4, we compare these knot properties with the predictions of various models for the formation of knots, their particle acceleration, and the jet structure. Finally, we outline the most likely processes for forming knots in Cen A in Section 5.

2. DATA

In this work, we use both new and archival VLA radio data at 4.8 GHz, 8.4 GHz, and 22 GHz observed over almost 20 years. Cen A has been observed at 4.8 GHz with the VLA since 1983 and at 8.4 GHz since 1991, including six monitoring observations taken by us since 2002 at roughly 18 month intervals. We also present new 22 GHz data taken in 2007 as part of a multi-frequency program (AG0754) where quasi-simultaneous observations of the jet knots were taken in these three radio frequencies timed to coincide with *Chandra* X-ray observations. The details of these radio data are shown in Table 1. All these data were observed with two intermediate frequencies (IFs) with beamwidths of 50 MHz. The radio frequencies used in this paper and in Table 1 are the average values for the two IFs. All the radio data were reduced in AIPS using the standard method. The data were phase, flux, and polarization calibrated before being split into a single source file. As our flux calibrator, 3C286, is resolved, we followed the recommended method of using a model during the flux calibration. For an initial approximation, the Cen A data were calibrated with a point-source model before being self-calibrated in phase to the point where no further improvement was noticed. The data were then amplitude and phase self-calibrated and baseline calibrated using the same method as Hardcastle et al. (2003). The radio data were translated to the published coordinates for the core of Cen A (Ma et al. 1998) in the *uv* plane using *uvfix* and *puthead*. The radio jet with all the radio knots labeled is shown in Figure 1; this image is the combination of all the 8.4 GHz radio images, individually scaled by the weighted mean of the rms background.

Cen A has also been observed in the X-ray with *Chandra* 10 times since 1999 (observations summarized in Table 2). These X-ray data span eight years and were taken in such a way that the jet is unaffected by the chip gaps or the read-out streak of the core. With the high resolution provided by *Chandra*, these well-sampled data give us a unique opportunity to study the temporal properties of the jet and its knots. The most recent data, taken in 2007, were part of a *Chandra* Very Large Program (VLP: P.I. R. P. Kraft), consisting of 6×100 ks observations, giving us a combined livetime of 719 ks when merged with the earlier data. A summary of the reduction processes is given in Sivakoff et al. (2008) and Hardcastle et al. (2007). These VLP data have been used thus far to study the X-ray binaries in Cen A (Jordán et al. 2007; Sivakoff et al. 2008; Voss et al. 2009), the properties of its hot gas (Kraft et al. 2008; Croston et al. 2009) and of its jet (Hardcastle et al. 2007; Worrall et al. 2008). The merged X-ray data set, in the energy range 0.4–2.5 keV, is shown in Figure 2 with the X-ray knots labeled.

X-ray spectra were extracted for each of the jet knots (see Section 3) and the diffuse regions in the jet, using the CIAO task *specextract*, which also calculated the response files, while *psextract* was used to extract the spectra of all the point sources in the field for a comparative sample (Section 3.4). As some of the jet knots are clearly extended in the X-ray data (and we wanted to compare with other more extended jet features), we used *specextract* (appropriate for extended sources) for all of the jet knots for consistency; however, we used *psextract* for the comparison sample, as it consisted entirely of unresolved point sources. As the jet knots are compact sources embedded in the diffuse jet and lobe material, local, on-source annular regions

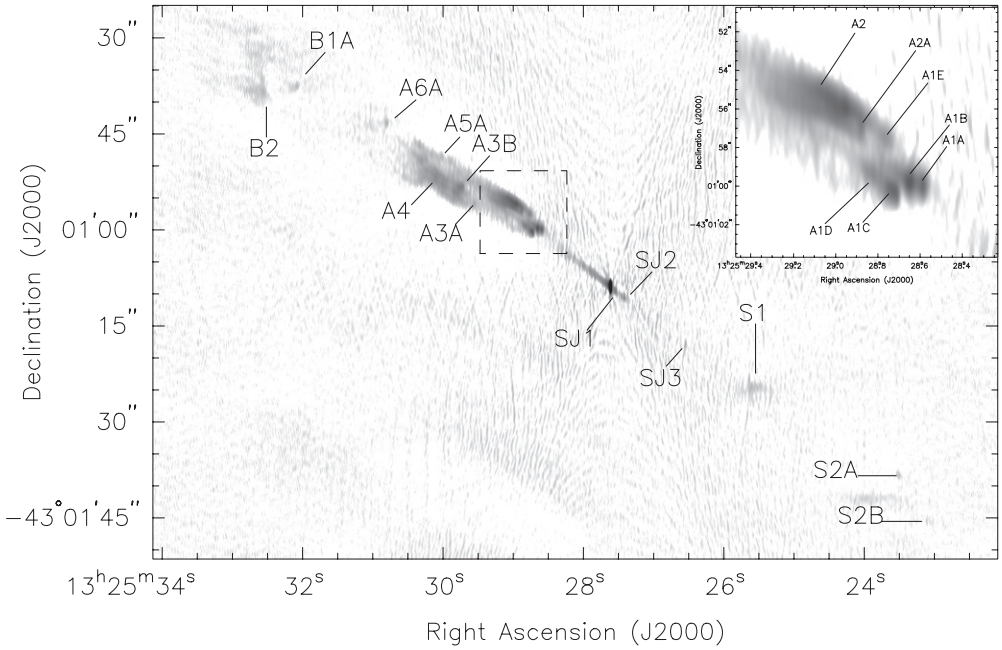

Figure 1. Stacked 8.4 GHz A-configuration radio image of the inner jet in Cen A showing the jet and counterjet with the 19 radio knots labeled as well as the A2 diffuse region. The dashed box indicates the location of the inset panel (top left), which shows the A1 and A2 groups of knots. In both the main image and the inset, black corresponds to 0.1 Jy beam^{-1}; however, white corresponds to 0.07 mJy beam^{-1} and 0.2 mJy beam^{-1}, respectively. The beam is 0.2 × 0.8 arcsec.

Table 1
Radio Observation Details

Frequency (GHz)	VLA Config.	Date	Program ID	Dynamic Range (arcsec)	Res. (mJy beam^{-1})	rms Noise
4.8164	A	1983 Oct 28	AB0257	18300:1	1.23 × 0.33	0.042
4.8164	A	1986 Mar 16	AF0113	6570:1	1.41 × 0.36	0.264
4.8851	A	1992 Dec 18	AK0316	27300:1	1.63 × 0.38	0.025
4.8851	A	2007 Jun 7	AG0754	14800:1	1.58 × 0.38	0.349
8.4399	A	1991 Jan 2	AB0587	91800:1	0.78 × 0.20	0.071
8.4601	A	2002 Mar 3	AH0764	95700:1	0.76 × 0.20	0.067
8.4601	A+PT	2003 Jun 2	AH0813	32300:1	0.79 × 0.21	0.233
8.4601	A+PT	2004 Dec 14	AH0855	77300:1	0.76 × 0.19	0.082
8.4601	A+PT	2006 Feb 18	AH0892	67500:1	0.65 × 0.15	0.103
8.4601	A	2007 Jun 4	AG0754	92200:1	0.82 × 0.23	0.069
8.4061	A	2008 Dec 20	AG0798	78800:1	0.82 × 0.21	0.069
22.4851	A	2007 Jun 16	AG0754	14800:1	0.72 × 0.19	0.457
	B	2007 Dec 21				

Table 2
X-ray Observation Details

Observation (#)	Date	Detector	Exposure (s)
0316	1999 Dec 5	ACIS-I	26493
0962	2000 May 17	ACIS-I	36505
2978	2002 Sep 3	ACIS-S	44589
3965	2003 Sep 14	ACIS-S	49518
7797	2007 Mar 22	ACIS-I	96888
7798	2007 Mar 27	ACIS-I	90839
7799	2007 Mar 30	ACIS-I	94783
7800	2007 Apr 17	ACIS-I	90843
8489	2007 May 8	ACIS-I	93936
8490	2007 May 30	ACIS-I	94425

were used for the background subtraction. The spectra were then binned to 20 counts per channel after background subtraction, ignoring the first 28 channels that correspond to energies below 0.4 keV. The X-ray fitting was carried out using XSPEC 11.3 in the energy range 0.4–7.0 keV where the *Chandra* response is well calibrated. In this analysis, *Chandra* data processing was done using CIAO version 3.4 and CALDB version 3.3.0.1. We define the spectral index such that flux density $S \propto \nu^{-\alpha}$, and the photon index as $\Gamma = 1 + \alpha$. The errors in this work are 1σ errors unless otherwise stated.

3. RESULTS

Our radio and X-ray data sets allow us to analyze the temporal behavior of the knots in Cen A's jet. We first consider whether the knots are really jet related or whether some of them are coincidentally positioned foreground or background objects (Section 3.1). Next, in Section 3.2, we examine the multi-frequency radio and X-ray data to determine whether inverse-Compton emission (IC) is significant in the jet knots before establishing the proper motions of the knots in Section 3.3. We then consider the radio, polarization, and X-ray variability of the knots (Sections 3.4 and 3.5). We also measure the radio spectral indices, X-ray spectral indices, and X-ray/radio flux density

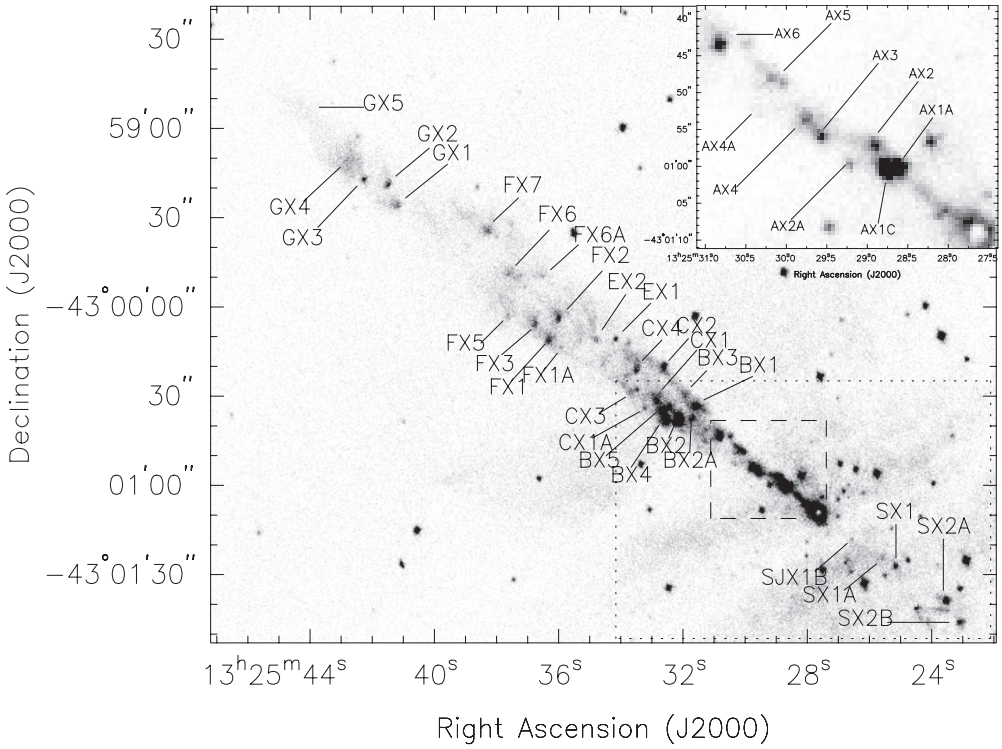

Figure 2. X-ray image of the jet in Cen A with all 40 detected X-ray knots labeled. The X-ray image is in the energy range 0.4–2.5 keV and shows only the portion of the data which includes the jet and counterjet. The dotted line indicates the extent of the radio jet shown in Figure 1 and the dashed line indicates the position of the inset (top left), which shows the A group of X-ray knots. In the larger image, black corresponds to 28 counts pixel^{-1} (0.4–2.5 keV) and in the inset, black corresponds to 150 counts pixel^{-1} (0.4–2.5 keV). In both images, white corresponds to 0 counts pixel^{-1}. In both images, the pixel size is 0.07 arcsec pixel^{-1}.

ratio to determine the broad spectra of the knots (Sections 3.6 and 3.7). Combining these properties provides us with evidence to test models for particle acceleration in the jet. We also investigate whether any of the knot properties depend on the position of the knot in the jet, following up previous work by Hardcastle et al. (2007) and Worrall et al. (2008).

We combined all of our 8.4 GHz radio data and all the X-ray observations to make deep, high dynamic range, radio and X-ray maps shown in Figures 1 and 2. These maps allowed us to make a definitive list of all the radio and X-ray knots in the jet. The 19 radio knots investigated in this work are mostly those defined by Hardcastle et al. (2003) with the addition of two knots, located downstream of the previously detected A1 knots. These knots were present in previous observations but were considered to be diffuse downstream emission. However, in the more recent observations, they appear much more compact, so have been designated A1D and A1E, and are investigated in this work. In the 8.4 GHz radio maps, where the resolution is 0.8 × 0.2 arcsec, we find bandwidth smearing significantly affects knots beyond 140 arcsec which is beyond the F-group of X-ray knots so does not affect the radio knots in the A-configuration maps. We also note that the radio jet is within the primary beam of the VLA at all of our observed frequencies so primary beam attenuation is not corrected for. Time-averaging smearing is also not significant at these scales. We examined maps which extend to the inner edge of the inner lobes (including the B-array VLA data of Hardcastle et al. 2003) and we find no evidence of additional compact radio knots beyond the B-group radio knots already detected. Bandwidth smearing does not affect these images until beyond the jet. The absence of knots at large distances from the nucleus will be discussed further in Section 4.1.3.

The 40 X-ray knots used in this work are a combination of those identified by Kraft et al. (2002) and Hardcastle et al. (2003) with independently selected central coordinates. The coordinates were optimized so that a fixed radius of 3 arcsec includes the majority of the emission associated with the knot and is larger than the point-spread function (PSF) in all observations. In the cases where the knot is close to the pointing center, this fixed radius slightly overestimates the flux from the knot including some background, although the majority of this excess is removed during the background subtraction. We compared the X-ray flux of our fixed-radius regions with the flux measured using regions with radii that were modeled using the PSF and found that the changes in the light curve reflected the changes in the PSF between observations. We therefore use fixed-radii regions to eliminate this effect. We use annular background regions to account for spatial variations in the underlying diffuse emission. We have investigated the systematic uncertainty due to variation in the surface brightness within these annular background regions and find that the contribution to the X-ray flux density is negligible (less than 1%), even in the worst affected knots. As AX1A and AX1C are very close together, manually sized regions were used, adjusted to include as much of the emission as possible, without including too much emission from the neighboring knot. The spectral properties of all the X-ray knots are shown in Table 3.

3.1. Point-source Contamination

Kraft et al. (2002) investigated whether some of the apparent X-ray knots could be low-mass X-ray binaries (LMXBs) in Cen A or background active galactic nuclei (AGNs). They simulated point sources using the first of the *Chandra* X-ray

Table 3
Spectral Properties of the X-ray Knots

Knot	Flux Density[a] 1 keV (nJy)	Spectral Index α_X	N_H ($\times 10^{22}$ cm^{-3})
AX1A	10.65 ± 1.64	1.08 ± 0.04	0.51 ± 0.02
AX1C	21.43 ± 2.97	1.06 ± 0.04	0.52 ± 0.02
AX2	9.29 ± 0.54	0.77 ± 0.07	0.55 ± 0.04
AX2A	3.19 ± 0.96	0.56[b]	0.084[b]
AX3	4.02 ± 0.39	0.78 ± 0.16	0.40 ± 0.07
AX4	4.98 ± 0.28	0.94 ± 0.16	0.45 ± 0.04
AX4A	0.30 ± 0.03	0.48[b]	0.084[b]
AX5	6.60 ± 0.39	0.59 ± 0.09	0.59 ± 0.08
AX6	9.39 ± 0.35	0.51 ± 0.06	0.59 ± 0.05
BX1	3.69 ± 0.27	0.83 ± 0.11	0.12 ± 0.02
BX2	19.39 ± 0.97	0.63 ± 0.02	0.11 ± 0.01
BX2A	1.44 ± 0.12	0.58 ± 0.12	0.084[b]
BX3	2.02 ± 0.17	1.40 ± 0.35	0.15 ± 0.10
BX4	4.94 ± 0.30	0.91 ± 0.06	0.084[b]
BX5	3.06 ± 0.23	1.13 ± 0.15	0.10 ± 0.03
CX1	2.36 ± 0.20	1.23 ± 0.17	0.084[b]
CX1A	0.97 ± 0.07	2.20[b]	0.084[b]
CX2	3.59 ± 0.37	0.79 ± 0.06	0.12 ± 0.04
CX3	0.82 ± 0.09	0.63[b]	0.084[b]
CX4	1.09 ± 0.18	0.54 ± 0.20	0.084[b]
EX1	0.78 ± 0.14	0.60[b]	0.084[b]
EX2	0.58 ± 0.06	0.60[b]	0.084[b]
FX1	1.92 ± 0.11	0.77 ± 0.12	0.084[b]
FX1A	0.34 ± 0.09	0.70[b]	0.084[b]
FX2	2.11 ± 0.25	1.28 ± 0.27	0.12 ± 0.09
FX3	1.36 ± 0.16	1.06 ± 0.30	0.084[b]
FX5	0.52 ± 0.03	1.20[b]	0.084[b]
FX6	0.77 ± 0.08	1.56[b]	0.084[b]
FX6A	0.47 ± 0.06	1.20[b]	0.084[b]
FX7	1.25 ± 0.18	1.07 ± 0.17	0.084[b]
GX1	1.10 ± 0.15	0.87 ± 0.19	0.084[b]
GX2	1.00 ± 0.13	0.63 ± 0.14	0.084[b]
GX3	1.21 ± 0.30	1.24 ± 0.50	0.15 ± 0.11
GX4	0.61 ± 0.10	1.20[b]	0.084[b]
GX5	0.13 ± 0.03	1.20[b]	0.084[b]

Notes.
[a] Weighted mean 1 keV X-ray flux density of the six 100 ks observations taken in 2007.
[b] Parameter fixed as too faint for joint fitting; the spectral index is an average of the local fitted indices and the nH is the Galactic value.

data sets used in this work (ObsID 0316) to determine whether the compact knots were point-like enough in their observations to be confused with LMXBs and found many that are consistent. They also considered the radial surface-density distribution of X-ray sources in Cen A, concluding that they expected ∼3 of the knots or sources to be X-ray binaries within Cen A unrelated to the jet.

It has been shown (see Fabbiano 2006 for a review) that a significant fraction of LMXBs observed in early-type galaxies with *Chandra* is associated with globular clusters (GCs). It has recently been confirmed that 41 X-ray point sources in our Cen A data are associated with GCs within Cen A (Woodley et al. 2008; Jordán et al. 2007; Voss et al. 2009). We examined *Spitzer*/IRAC 3.6 and 8 μm IR maps (Brookes et al. 2006; Hardcastle et al. 2006) to check for IR counterparts to our jet knots, which would indicate a coincident GC and found a compact IR source for GX3. We also checked the GC catalogue by Jordán et al. (2007) and found a GC coincident with GX3 only. Although we do not expect all LMXBs to reside in GCs, we can rule out any knot that has IR emission as likely to be a LMXB due to its association with a probable GC. Since >70% of all LMXBs identified with GCs lie in the redder GCs, those with a higher (near-solar) metal abundance (e.g., Woodley et al. 2008; Posson-Brown et al. 2009), the latter would actually be more readily detectable in the near-IR *Spitzer*/IRAC observations than in ground-based optical images.

The X-ray knots AX2A and SX1 are compact X-ray sources with no compact or diffuse radio emission, and they lie outside the boundaries of the detected radio jet and counterjet. However, the X-ray flux variability of AX2A is substantially different from that of SX1; it was undetected until 2007 when it flared to 3 nJy, and it has not varied significantly since. AX2A may therefore be a genuine new X-ray knot rather than a LMXB, so is considered further in Section 4.

Contamination from background AGN is highly unlikely; these would appear as point sources, possibly with optical counterparts and generally with flatter X-ray spectra (typical unabsorbed X-ray AGN spectra have spectral indices 1.09 ± 0.08, Mainieri et al. 2007). We have also calculated the number of AGN we expect in the jet using the background $\log N - \log S$ method described by Moretti et al. (2003) and find only a 33% chance of finding an AGN in our jet.

3.2. Emission Mechanism

Using the three frequencies of radio data observed in 2007, we fitted a synchrotron model to the radio emission from the inner A-group knots, which has allowed us to predict the X-ray emission we would expect from synchrotron self-Compton emission (SSC) and from the IC scattering of the cosmic microwave background (IC/CMB) and of the galaxies optical star light (IC/SL). We used the sizes measured by Tingay & Lenc (2009) to estimate the emitting volume of the stationary knots, which appear to have compact cores, combining the volumes of the substructures in the cases of A1A and A2A. We used the radio fluxes measured from radio maps matched to the resolution of the 22 GHz data (1.80 × 0.40 arcsec) and the weighted mean, 1 keV X-ray flux density from the six 2007 X-ray observations. At equipartition magnetic field strengths, the observed X-ray emission is much greater than the predicted X-ray flux density, which is dominated by SSC for the stationary knots, A1A, A1C, and A2A. If we assume the SSC model is dominant in the X-ray regime, we find that the magnetic field strengths required for the observed X-ray emission, for the stationary knots, are a factor of 500–600 weaker than the equipartition values. This is also true for the knots that are not detected by Tingay & Lenc (2009) and that are unresolved in our data; a limit on the sizes was used to find the limits on the equipartition magnetic field strengths, and the internal energies and pressures of the knots. Table 4 shows the radius of the emitting volume, the radio and 1 keV X-ray flux densities, the equipartition magnetic field strengths, B_{eq}, and the required magnetic field strength for SSC-dominated X-ray emission, B_{SSC}, of the A-group of knots.

In other features, such as the hotspots in FR II radio galaxies, the magnetic field strengths required for the observed X-ray are only slightly less than the equipartition values (factors of 3–5; Hardcastle et al. 2004; Kataoka & Stawarz 2005). The much larger departure from equipartition required for IC to be significant in the Cen A knots, combined with the steepness of the spectral indices for these knots ($\alpha_X > \alpha_{IC} \sim 0.5$) suggests that IC emission is not significant in the X-ray for the majority of the jet knots. We therefore assume that the X-rays from the knots are synchrotron emission in the remainder of this work.

Using the equipartition magnetic field strengths, we were able to estimate the total energy density of the knots and find

Table 4
Emission Model Parameters for the Inner A-group Knots

Knot	Radius	Flux Density				X-ray Lifetime	Magnetic Field Strength		Pressure
	(pc)	4.8 GHz (mJy)	8.4 GHz (mJy)	22 GHz (mJy)	1 keV X-ray (nJy)	τ_{1keV} (yr)	B_{eq} (nT)	B_{IC} (nT)	P_{int} (nPa)
A1A/AX1A	2.017	20.10 ± 4.26	12.27 ± 2.04	5.32 ± 0.98	10.65 ± 1.64	5.61	69.3	0.119	0.955
A1B	< 6.586	46.92 ± 5.58	29.44 ± 2.67	13.83 ± 1.28	< 19.38	17.63	32.3	> 0.125	0.937
A1C/AX1C	2.293	41.45 ± 5.66	25.33 ± 2.70	12.32 ± 1.30	21.43 ± 2.97	4.86	76.3	0.135	1.546
A2A/AX2	2.727	37.13 ± 5.82	15.57 ± 2.78	6.32 ± 1.33	9.29 ± 0.54	7.46	57.3	0.119	0.871
B1A/BX2	15.300	2.64 ± 0.64	0.93 ± 0.61	-	19.39 ± 0.97	30.89	22.2	0.038	0.131

that the internal pressures of these knots are of the order of 1 nPa, which is much higher than the pressure in the surrounding diffuse material. This is also evident from the higher surface brightness of the knots, which is directly related to the internal energy of the knot material.

3.3. Proper Motions

The results of Hardcastle et al. (2003) were based on only the first two epochs of radio data. With these data, they were able to establish the bulk flow speed of the jet ($\sim 0.5c$) and also demonstrated that some of the knots move along the jet (A1B, A2, A3B, and A4) while others were consistent with being stationary (A1A, A1C, A2A, A3A, A5A, B1A, SJ1, SJ2, SJ3, S2A, and S2B). With our multi-epoch data, we can improve on the accuracy with which the proper motions are measured. We used maps with a matched resolution of 0.80×0.20 arcsec for these measurements.

Our approach to fitting speeds was to use a modified version of the shift-and-fit method of Walker (1997), as used in a simpler form by Hardcastle et al. (2003). As we have more than two maps, we attempted to fit a velocity vector, consisting of an angular speed and direction, to each knot. (More complex models are not justified by the quality of the data.) To use the shift-and-fit method, we selected a reference image at a particular epoch. For a given trial value of the angular velocity vector, the appropriate part of this image was then shifted (using a bicubic polynomial interpolation) to the position implied for all the other epochs, the difference of the two images was formed, and the contribution to χ^2 was calculated using estimates of the local on-source noise in both maps. The total χ^2 over all non-reference images was minimized using a Markov–Chain Monte Carlo algorithm (briefly described by Croston et al. 2008) which allows the efficient exploration of parameter space. A Jefferys (scale-invariant) prior was used for the magnitude of the angular velocity vector to avoid bias toward large values. In principle this algorithm also allows an efficient determination of the uncertainties (formally the credible intervals) on the fitted parameters. However, we found that these errors were dominated by the systematic uncertainties due to the choice of reference image; in weak knots a fortuitous distortion in the reference image can give the appearance of a proper motion that is not actually present. To remedy this, we carried out the fits for a given knot using each of our seven radio images in turn as the reference image. Only knots in which consistent, non-zero motions are detected for all choices of the reference image are considered to be moving. In these cases, our best estimate of the speed of the motion is the median of the Bayesian estimates of the angular speed for each choice of reference image, and the range of speeds returned under different choices of the reference image gives us an estimate of the systematic uncertainties in the result. Where the velocities are inconsistent, we have taken the upper limit to be the largest velocity in this range.

This approach detected apparent motions in six of the radio knots as well as in the diffuse material downstream of the A2A knot (the regions downstream of A2A are labeled A2B, A2C, and A2D in the following sections). To check that these motions are sensible, we verified the motion visually. We found that two of these knots, A1C and A2A, are actually stationary, and we attribute the detected proper motion to the evolution of the knot; A1C appears to grow downstream while A2A's front edge is stationary with diffuse material appearing to break off and move downstream from this knot toward A2B, A2C, and A2D (all consistent with Hardcastle et al. 2003). The visual checks also rule out the apparent motion in SJ1 as its proximity to the bright core means its shape is affected by artifacts. We are left with three knots moving in the jet: A1B, A1E, and A3B (their velocities are plotted as vectors in Figure 3 and shown in Table 5 with the limits for the stationary knots). This approach is more robust than that of Hardcastle et al. (2003) as it considers all seven epochs of our radio data, reducing the errors on the proper motions of the moving knots, and we have constrained the speeds of the other knots that had no previously detected proper motions.

It is worth noting here that A1B and A1E have no X-ray emission associated with them while the region A3B can be described as consisting of three subregions in the radio with a diffuse X-ray counterpart, possibly breaking any correlation between compact, radio-only knots, and proper motions.

We have also determined the directions of travel for the well-established moving knots (Table 5). The axis of the inner, hundred-parsec-scale jet has a position angle (P.A.) of 54.°1 east of north from the core, and its extrapolation provides a good estimate of the axis of much of the outer jet. The moving knots all travel in directions eastward of this axis. They also all belong to the A-group of knots and, on closer inspection of this section of the jet, we find that it also deviates eastward to greater P.A.s. The jet axis in this region has a P.A. of 62.°3. Two of our three knots move in a direction consistent with this, within 3σ errors. If the jet motion was purely conical, expanding directly away from the core, the motion of the knots should be radial, but we find that the directions of motion do not match the knot P.A.'s. The ridge line through the A-group knots may actually follow the regions of highest radio surface brightness, swinging from north of P.A. 54.°1 at A2 to south of it at A3 and A4. In Figure 4, deviations of the knot P.A.'s from 54.°1 are plotted against distance from the core, clearly showing this swing in the ridge line. We can only conclude that the fluid flow along the jet is neither laminar nor in a straight line away from the core, consistent with a complex flow.

The median speeds of the remaining radio knots are generally smaller than the speed of the slowest knot with a definite

Table 5
Summary of X-ray and Radio Knot Behavior

Name		Radio Varying?		X-ray	Polarization		Proper Motion					
X-ray	Radio	4.8 GHz	8.4 GHz	Varying?	Degree of?	Angle of?	Y/N	Median v (c)	Upper Limit (c)	θ_v (deg)	$v_{\rm R.A.}$ (c)	$v_{\rm Decl.}$ (c)
AX1A	A1A	Y	N	N	Y	Y	N	0.002	<0.05		<0.04	<0.00
...	A1B	N	Y	-	N	N	Y	$0.534^{+0.06}_{-0.02}$		$67.40^{+3.70}_{-2.13}$	$0.50^{+0.06}_{-0.02}$	$0.21^{+0.01}_{-0.02}$
AX1C	A1C	Y	Y	Y	N	Y	N	0.076	<0.14		<0.14	<0.11
...	A1D	N	Y	-	N	Y	I	0.095	<0.58		<0.49	<0.30
...	A1E	Y	N	-	N	N	Y	$0.338^{+0.22}_{-0.15}$		$54.18^{+30.12}_{-25.12}$	$0.28^{+0.19}_{-0.08}$	$0.25^{+0.16}_{-0.16}$
AX2	A2A	N	N	N	N	Y	N	0.164	<0.24		<0.09	<0.24
AX3	A3A	Y	N	N	N	N	N	0.031	<0.05		<0.03	<0.01
AX4	A3B	N	N	N	N	N	Y	$0.802^{+0.15}_{-0.09}$		$71.17^{+11.94}_{-11.76}$	$0.79^{+0.19}_{-0.09}$	$0.27^{+0.14}_{-0.15}$
...	A4	N	N	-	N	Y	I	0.928	<1.00		<1.00	<0.32
AX5	A5A	N	N	N	N	N	I	0.016	<0.34		<0.26	<0.23
AX6	A6A	N	N	N	N	N	I	0.370	<0.62		<0.51	<0.36
BX2	B1A	Y	Y	Y	N	N	I	0.049	<0.74		<0.69	<0.27
BX4	B2	N	Y	N	Y	N	I	1.000	<1.00		<1.00	<1.00
...	SJ1	Y	Y	-	Y	N	I	0.371	<0.81		<0.38	<0.72
...	SJ2	N	N	-	N	N	I	0.193	<0.59		<0.22	<0.55
SJX1B	SJ3	N	N	N	N	N	I	0.213	<0.90		<0.47	<0.88
SX1A	S1	Y	Y	N	Y	N	I	0.238	<0.83		<0.79	<0.24
SX2A	S2A	N	Y	N	N	N	I	0.250	<0.37		<0.30	<0.24
SX2B	S2B	N	N	N	Y	N	I	0.305	<0.60		<0.55	<0.49

Notes. AX2A, EX1, FX1A, GX5, and SX1 vary in the X-ray and do not have radio counterparts. AX4A, BX1, BX3, BX5, CX1, CX2, CX3, CX4, EX2, FX1, FX2, FX3, FX5, FX6, FX6A, FX7, GX1, GX2, GX3, and GX4 do not vary in the X-ray and do not have radio counterparts. The knot proper motions are classified as moving (Y), stationary (N), and inconclusive (I).

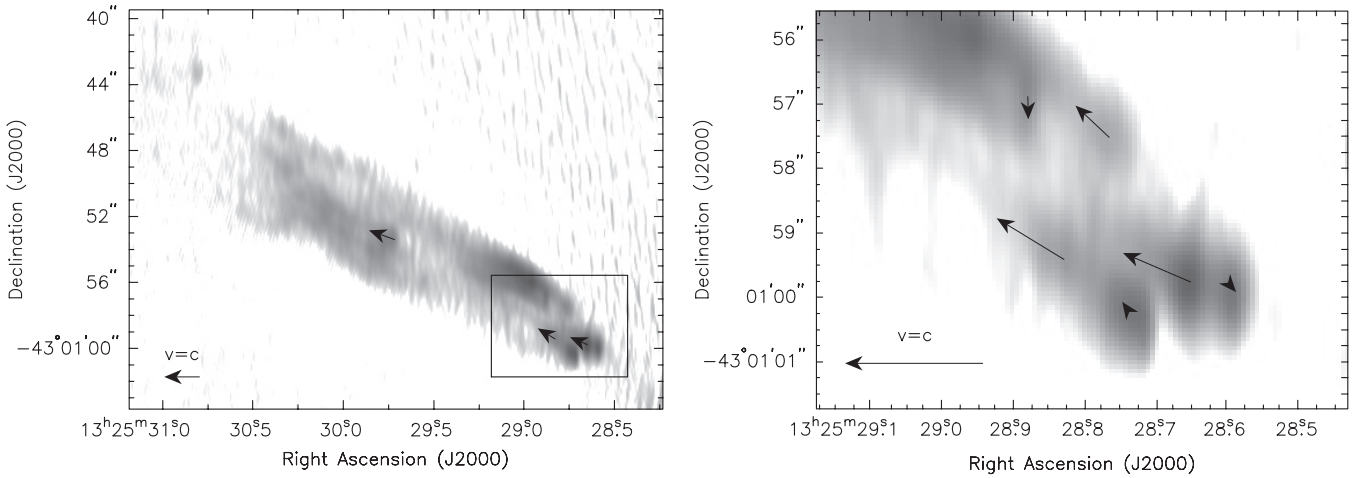

Figure 3. Velocity vectors for the moving knots in Cen A, with the composite 8.4 GHz radio map convolved to a resolution of 0.8 × 0.2 arcsec showing the well-established velocities for the A-group of radio knots (left panel), and the mean velocities of the A1 and A2 knots are shown in the right panel. The region included in the right image is shown with the box on the left image. Black corresponds to 0.1 Jy and white corresponds to 0.1 mJy in the left panel and 0.5 mJy in the right panel. A velocity of 1c is shown in the bottom left corner of these images.

detection, A1E, ($v/c \sim 0.34$), but in most cases the upper limits exceed 0.5c, allowing the knots to be moving. We require better data to establish whether this is the case, so for the remainder of this work, we have considered those with well-established velocities to be moving, those with low median speeds ($< 0.2c$), and low upper limits to be stationary, and we classify the others as inconclusive. In Table 5, these classifications are indicated by Y, N, and I, respectively. We discuss the association between the motions of the knots and their other properties in Section 4.1.5.

3.4. Flux Variability

Another important property that can be measured from our multi-epoch radio and X-ray data is flux variability. Utilizing the multi-epoch 8.4 GHz radio data, we have been able to monitor the radio flux variability over the last 17 years. We used radio maps of matched resolution (0.80 × 0.20 arcsec) for this analysis to eliminate any flux variation due to varying PSF. The initial light curves for the radio knots showed a systematic variation of up to ±10% common to all knots, which we attributed to differences in the flux calibration, so we normalized the radio fluxes using a weighted mean of the brightest compact knots (A1A, A1B, A1C, A2A, A3B, and A4). We chose these knots as the others are weaker and/or more diffuse, and would therefore introduce large uncertainties in our weighted mean value. We also excluded SJ1, which shows strong variation since 2004. The core was not used in this normalization as it is known to vary. The normalized fluxes are shown in Table 6. We fitted a

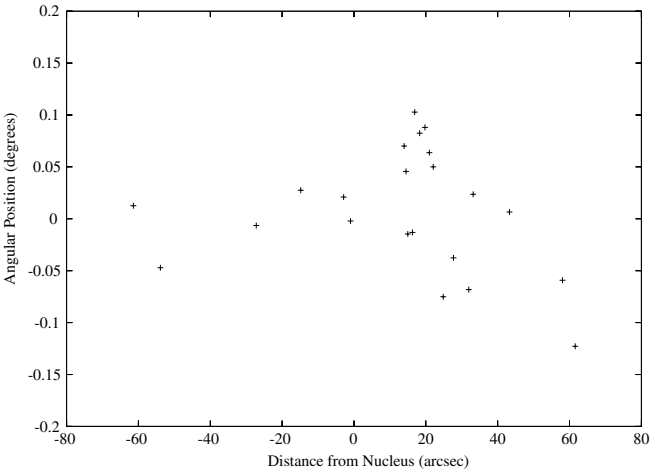

Figure 4. Offset between the P.A. of the jet in Cen A (54°) and the transverse position of the radio knots as a function of the projected distance from the nucleus for the knots in the jet and counterjet (negative distances). The knots do not appear to lie at the P.A. 54° for the entire length of the jet.

constant to these radio light curves and minimized the χ^2 to determine whether the radio fluxes are at all variable, with a reduced $\chi^2 < 2.80$ being the threshold for a constant radio light curve (99% confidence for 6 degrees of freedom (dof)). We detect radio variability at this confidence level in 9 of the 19 radio knots (49.4%). The light curves of these varying knots are shown in the Appendix; Figures 12 and 13 show the light curves for those radio knots with X-ray counterparts, and Figures 14 and 15 show the radio and X-ray light curves for the radio-only knots. The most noticeable variation is in the counterjet knot SJ1, which has increased in flux by a factor of 3 since 1991. Three of these radio variable knots show fluctuations on yearly timescales (B2, S1, and S2A), while the remaining four split into two increasing (A1C and SJ1) and two decreasing (A1B and A1D) gradually over the 17 years.

We also considered variability in the 4.8 GHz data but as we have only four observations over 24 years at irregular intervals, we cannot comment on any short-term variability. These light curves are all broadly consistent with the 8.4 GHz light curves, an example of which is shown in the Appendix, Figures 14 and 15. Accepting a reduced $\chi^2 < 3.78$ as a constant light curve (99% confidence for 3 dof) we find six radio knots with some degree of variability at 4.8 GHz, half of which are also variable in the 8.4 GHz data with the detected 8.4 GHz variable knots, which is not to say that those which are apparently constant do not agree with the 8.4 GHz variability. This is particularly evident in the SJ1 data, as only two observations overlap with the time baseline of the 8.4 GHz data; these data could be interpreted as decreasing while the 4.8 GHz data increases, but there are too few data to draw any conclusion from the 4.8 GHz light curves. The dynamic ranges of these 4.8 GHz data are much lower than our 8.4 GHz data, so they are subject to much larger systematic errors.

We also detected long- and short-term X-ray variability. Combined with the radio variability, this allows us to search for any changes in beaming or particle acceleration properties. We carried out a joint fit to all 10 X-ray data sets for all the X-ray knots, fitting a single photon index and column density for each knot, but allowing the normalizations to vary in order for any variations in the flux to be detected. The normalizations were converted to 1 keV flux densities so the light curves could be plotted including 1σ errors. We then fitted a constant to the light curves, minimizing the χ^2 to find the best fit. We were able to carry out a joint fit for 24/40 of the X-ray knots, 22 of which have a $\chi^2_{\rm red} < 1.10$. For the remaining knots where there were not enough counts for spectral fitting, we firstly determined whether there was a 3σ detection of the knot considering each observation separately. Where the knot was detected, we fixed the photon index to the average photon index of the nearby knots. The flux was then determined from the background subtracted counts and the model count rate from XSPEC. Where the knot was not detected, the 3σ limit was calculated.

Knots with a $\chi^2_{\rm red} > 2.41$ (99% confidence for 9 dof) are considered variable in the X-ray. We find that five X-ray knots vary (12.5%) in addition to AX2A and SX1 which are candidate LMXBs (see Section 3.1), three of which have varying radio counterparts. The light curves for the X-ray varying knots are shown in the Appendix; Figure 10 shows the X-ray only knots while those that have radio counterparts are shown in Figures 12 and 13.

To test whether the variability behavior is consistent with, or different from that of the non-jet point sources, we also extracted spectra for the off-jet point sources. We manually checked the results of *celldetect* to remove detections of image artifacts and the jet knots before running the same fitting using annular background regions. We detected 423 point sources, only 183 of which are detectable in all observations due to changes in the pointing and roll angle of *Chandra* for each observation causing slightly different regions of the sky being imaged. Although the PSF changes across the image for each observation, these point sources all lie within 5.5 arcmin of the core, so the changes in the PSF of each knot is not significant. However, the changes in PSF between each observation are more significant and are reflected in the light curves causing an apparent flux variability. To remove this effect from the light curves, we have used regions with a fixed radius of 3 arcsec for these point sources. We fitted a constant to the X-ray light curves of these point sources and found 105 show some degree of variability with 99% confidence (56.8% $\pm$ 10.3% of the point sources), a factor of 3 more than the jet X-ray knot population. In 41 instances, the background annulus contained zero counts so these were re-extracted with a larger background annulus to determine a limit. If we consider the point sources within 3.5 arcmin of the core, which limits us to the length of the jet from the core, we find that 76/141 point sources vary (53.9% $\pm$ 8.7%) and if we reduce the sample further to include only those on the east of the image, so those within 45° of the jet P.A., we find that 33/71 point sources vary (46.5% $\pm$ 5.7%). We can see that the effect of the PSF is not significant in these samples and we can conclude that we are looking at a group of different objects in the jet and not just coincidentally positioned X-ray binaries in most cases.

3.5. Polarimetry

If there is compression/rarefaction of the plasma in the knots, we would expect changes in the polarization, as the magnetic field is assumed to be frozen into the plasma. We can therefore use the polarization data to investigate any link between the activity of the knots with physical changes in the plasma. The coadded, matched resolution, Q and U images at 8.4 GHz were used to make a deep magnetic field vector map shown in Figure 5. We made the individual Stokes Q and U maps using the AIPS task *imagr*. There are artifacts around the core for all epochs, which we attribute to the limited accuracy of the correction calculated for the "leakage" terms determined

Table 6
Normalized Radio Knot Flux Densities at 8.4 GHz with Local, On-source Background Subtraction

	Flux (mJy)						
Knot	1991	2002	2003	2004	2006	2007	2008
A1A	20.72 ± 0.59	19.97 ± 1.09	20.98 ± 1.17	20.98 ± 1.32	21.76 ± 1.61	22.94 ± 1.50	20.67 ± 1.68
A1B	52.80 ± 0.77	46.05 ± 2.24	45.53 ± 2.26	46.04 ± 2.61	45.98 ± 3.09	46.33 ± 2.76	41.62 ± 3.18
A1C	34.44 ± 0.78	38.06 ± 1.91	38.77 ± 1.98	39.87 ± 2.31	41.28 ± 2.83	40.43 ± 2.47	41.25 ± 3.16
A1D	11.18 ± 0.55	8.98 ± 0.70	8.83 ± 0.75	8.23 ± 0.81	8.77 ± 0.97	8.47 ± 0.91	8.46 ± 0.92
A1E	8.25 ± 0.71	9.79 ± 0.86	10.06 ± 9.31	9.86 ± 1.03	10.08 ± 1.20	9.09 ± 1.12	10.27 ± 1.16
A2A	23.99 ± 0.80	24.03 ± 1.37	23.99 ± 1.43	24.19 ± 1.62	23.33 ± 1.86	22.88 ± 1.69	23.81 ± 2.00
A3A	3.96 ± 1.29	3.75 ± 1.36	4.12 ± 1.51	3.06 ± 1.54	2.88 ± 1.98	4.05 ± 1.91	3.26 ± 1.56
A3B	22.33 ± 1.63	21.02 ± 1.96	20.64 ± 2.10	18.59 ± 2.18	16.92 ± 2.70	18.29 ± 2.59	18.46 ± 2.37
A4	24.75 ± 1.92	28.35 ± 2.39	27.48 ± 2.56	27.17 ± 2.70	26.44 ± 3.37	25.98 ± 3.16	28.72 ± 3.11
A5A	1.08 ± 0.30	1.86 ± 0.35	2.06 ± 0.34	1.23 ± 0.35	1.15 ± 0.42	0.22 ± 0.51	1.81 ± 0.43
A6A	2.85 ± 0.49	2.72 ± 0.56	3.12 ± 0.54	2.04 ± 0.57	1.19 ± 0.67	1.66 ± 0.83	2.41 ± 0.68
B1A	1.59 ± 0.49	2.43 ± 0.25	2.95 ± 0.55	1.25 ± 0.22	1.61 ± 0.43	2.04 ± 0.12	2.15 ± 0.34
B2	3.86 ± 0.59	4.29 ± 0.34	4.99 ± 0.67	2.46 ± 0.28	5.68 ± 0.61	2.74 ± 1.38	4.05 ± 0.47
SJ1	5.37 ± 0.89	12.78 ± 0.74	10.85 ± 1.36	14.76 ± 1.25	16.49 ± 2.71	18.72 ± 1.41	20.04 ± 1.51
SJ2	2.44 ± 0.74	5.13 ± 0.45	4.58 ± 0.11	6.04 ± 0.88	1.71 ± 0.21	3.59 ± 0.84	4.89 ± 0.48
SJ3	0.55 ± 0.84	1.17 ± 0.44	1.73 ± 1.20	1.53 ± 2.37	1.42 ± 0.93	0.73 ± 0.37	0.77 ± 0.39
S1	4.28 ± 1.09	10.10 ± 0.61	10.26 ± 1.16	6.11 ± 1.02	9.74 ± 2.01	8.95 ± 1.86	10.40 ± 0.93
S2A	2.28 ± 0.34	1.18 ± 0.19	1.51 ± 0.39	0.16 ± 0.17	1.83 ± 0.35	1.17 ± 0.81	1.94 ± 0.26
S2B	0.82 ± 0.34	0.55 ± 0.18	0.30 ± 0.38	0.05 ± 0.17	1.09 ± 0.34	0.43 ± 0.81	0.61 ± 0.22

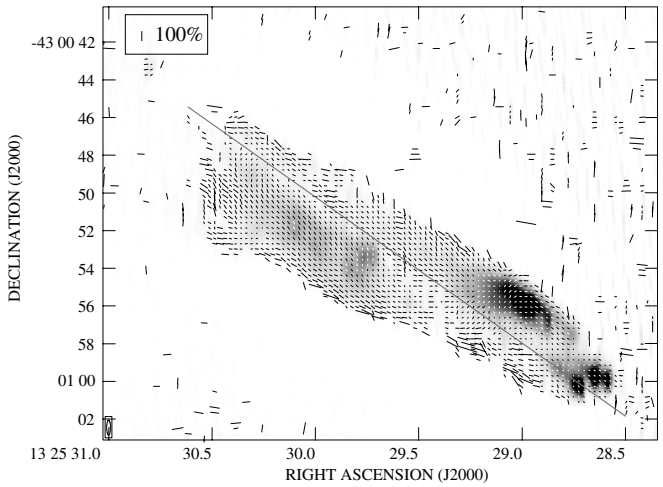

Figure 5. Radio polarization in the inner jet of Cen A showing the direction of the magnetic field vectors on a composite, Stokes I, 8.4 GHz radio map. The radio image is in the range 0.1–0.01 Jy and a vector 0.56 arcsec long represents 100%. The solid gray line highlights a possible axis of null polarization discussed in Section 3.5.

by *pcal*; only the 2003 data set is unusable due to higher noise in these Stokes Q and U images. The overall direction of the magnetic field is down the jet, consistent with what was found by Hardcastle et al. (2003) with no obvious change in the knots.

We detected a 3σ variation in residual maps of the Q and U Stokes parameters (2007–2002) in the A1 and A2 groups. The diffuse emission farther down the jet also showed evidence of low-level variability, but as this was uniform across the region it was attributed to differences in the flux calibration. We proceeded to measure the fluxes in Q, U, and I for these data, normalizing as described in Section 3.4. Comparing the total intensity (I), the angle of polarization ($\theta = \frac{1}{2}\arctan(U/Q)$, in this work we use the Q/U ratio as an approximation to this relationship) and the degree of polarization ($p = \sqrt{Q^2 + U^2}/I$) allowed us to identify variations due to a change in the total intensity, the polarization intensity, the polarization P.A. or those due to the proper motion of the knot.

As previous described, the majority of knots show only a low-level variation in total intensity; however, 4/19 show changes in the degree of polarization only: B2, SJ1, S1, and S2B (Appendix, Figure 17), and 6/19 show changes in the angle of polarization (Appendix, Figure 18) including two knots which show changes in both. We have to consider that one of these knots is moving, A1B, so the observed changes in polarization could be due to this movement. Excluding this moving knot, the number of knots varying only in the angle of polarization is unchanged, and we have one knot, A1A, which is changing in both. These results are compared with the total radio and X-ray flux variations in Section 3.8.

The A2 diffuse knot (A2B, A2C, and A2D) shows a change in the Q/U ratio indicating a change in the polarization angle across the region; however, there are no X-ray counterparts for any of these subregions and their radio spectral indices are consistent ($\alpha_{4.8}^{8.4} = 1.13 \pm 0.10$, 1.01 ± 0.16 and 1.22 ± 0.27, respectively). Only the central section, A2C, varies in total radio intensity but the entire region appears to be moving downstream away from A2A so this change in polarization may be due to the motion of this diffuse material. The detected variation in the A1 group knots A1A, A1B, and A1C cannot be attributed to motion of the knots, as only A1B is moving. In this instance, the observed polarization variability may be explained by compression and rarefaction of the knot material. We do not see any perpendicular field structure across any of the knots, which might be expected in a local shock model; however, this might be masked by complicated jet polarization structure. However, we do see systematic misalignments between the jet P.A. and the magnetic field associated with some jet features, notably A2 and A3B, which are highlighted in Figure 6, which shows the difference between the polarization angle and the P.A. of the jet. Clarke et al. (1992) found only a modest rotation measure (RM) in the inner lobes and jet, and only a slight change in the Faraday-corrected magnetic field vectors in their 6 cm (4.8 GHz) radio data, so we do not expect the effect of RM to be significant. We will discuss the effect of various models on the polarization of the knots further in Section 4.

It is interesting to note that there is an apparent null in the polarization which crosses the diffuse material of the A-group

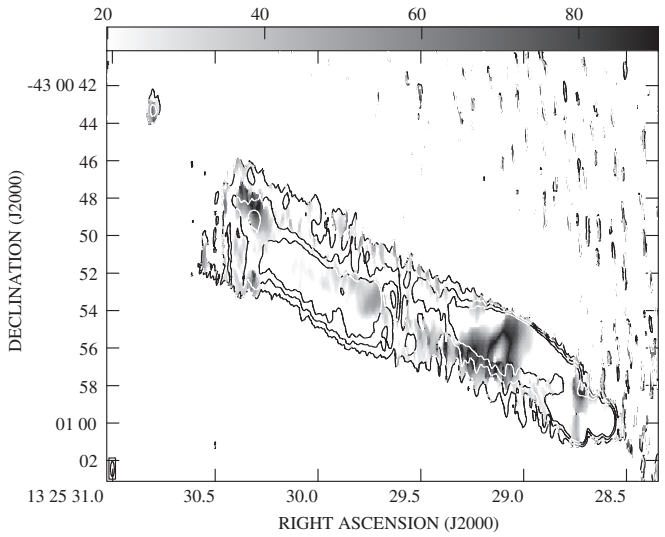

Figure 6. Grayscale map of the inner jet of Cen A showing the difference between the direction of the magnetic field vectors and the jet P.A. (51°.4) with total intensity contours at 3, 8, and 16 times the rms of the composite, Stokes *I* 8.4 GHz radio map, 8.23×10^{-5} Jy beam^{-1}. The grayscale image is in the range 20°–90° to emphasize structure in which the *B*-vectors are substantially misaligned with the jet.

region, indicated on Figure 5 by a gray solid line. This line extends to the core directly through the inner hundred-parsec-scale jet suggesting that it is associated with magnetic fields originating in or close to the core. This line also splits the bright A1 and A2 complexes from the A3 and A4 complexes. This could plausibly be a result of a helical jet field structure.

3.6. Spectral Indices

Hardcastle et al. (2007) and Worrall et al. (2008) investigated the X-ray spectrum of the jet in the longitudinal and transverse directions, respectively. Hardcastle et al. (2007) showed that the inner jet is dominated by knots, consistent with local particle acceleration at shocks, while further down the jet steeper-spectrum diffuse X-ray emission is more dominant. Worrall et al. (2008) found that in the knotty region beyond the A1 and A2 complexes and within 66 arcsec of the core, the weighted X-ray spectrum of knots closer to the jets axis (the "inner spine") is harder than that further off axis (the "inner sheath") ($\Delta\Gamma = 0.31 \pm 0.07$). This was interpreted as evidence that the jet speed is higher closer to the axis, with more kinetic energy available for producing a harder X-ray spectrum.

Here we compare the radio and X-ray spectral indices of individual knots with their longitudinal and transverse positions. We have measured the radio spectral indices for all of the radio knots; however, only 14 have well-established indices. In the X-ray, we have fitted spectral indices to 26 of the X-ray knots. We compared the X-ray spectral indices ($\alpha_X = \Gamma - 1$) of the jet-side knots, irrespective of whether they have counterparts, as a function of distance from the core (Figure 7), and of the offset between the angular position of the knot and the jet P.A. of 54°.1 (Figure 8).

All the X-ray spectral indices were consistent with those determined by Hardcastle et al. (2007) and consistent with synchrotron emission with $\alpha_X > 0.5$; the distances from the core of each knot were also consistent owing to the knot selection process. When we compared the measured spectral indices of all the radio and X-ray knots to the offset between the jet P.A. of 54°.1 and the angular position of the knot (Figure 8), we find a continuous distribution of X-ray spectral indices with no statistically significant correlation according to both a Kolmogorov–Smirnov and a Wilcoxon–Mann–Whitney test, although these tests do not take account of the errors on our spectral indices. We also considered the knots in each of the regions defined by Hardcastle et al. (2007) and find no correlation in these regions either. These comparisons will be discussed further in Section 4.4.

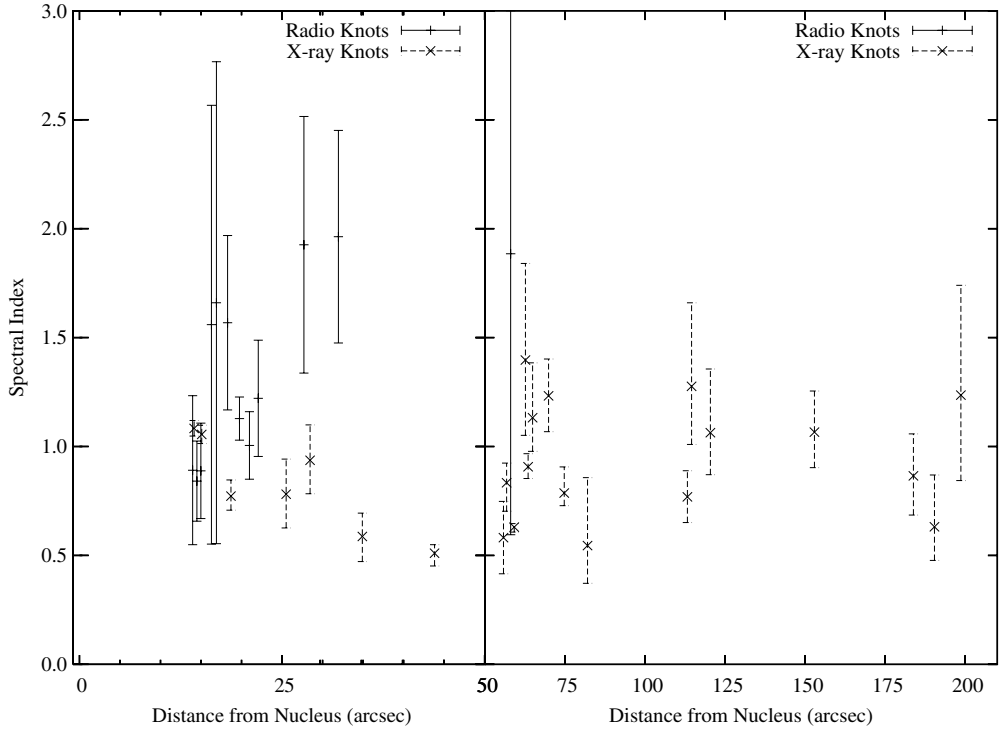

Figure 7. Radio spectral index, $\alpha_{4.8}^{8.4}$, (solid lines) and X-ray spectral index, α_X, (dashed lines) of knots in the jet of Cen A as a function of distance from the core. The left panel shows only the inner knots (up to 50 arcsec) and the right panel shows the rest of the jet knots.

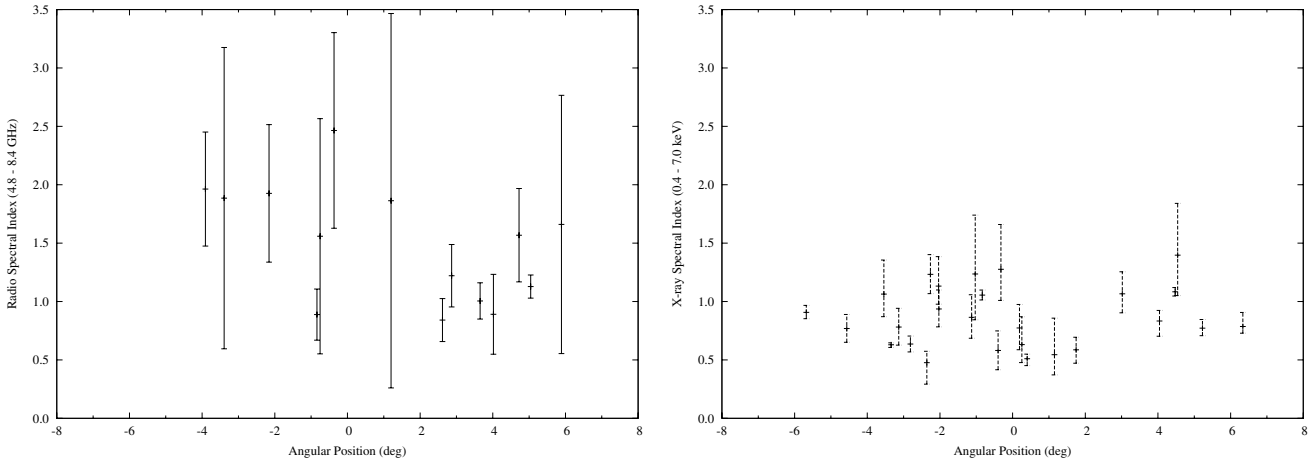

Figure 8. Radio spectral index, $\alpha_{4.8}^{8.4}$ (left panel, solid lines), and X-ray spectral index, α_X (right panel, dashed lines), of knots in the jet of Cen A as a function of offset between the angular position of the knot and the jet P.A. of 54°.1.

We have also found the weighted mean of the spectral indices for all of the knots within the regions defined by Worrall et al. (2008) as the "inner-spine" and "inner-sheath," $\alpha_X = 0.62 \pm 0.01$ and $\alpha_X = 0.89 \pm 0.05$, respectively, and agree with the findings of Worrall et al. of a harder weighted X-ray spectrum in the spine than in the sheath over the same length of jet (although $N_{\rm H}$ changes by a factor of 3, the absorption is fitted so does not affect the spectral indices). Within these regions, we have fitted spectral indices for 6/7 of those in the inner-spine; AX3, AX4, AX5, AX6, BX2, and BX5, and for 3/4 or those in the inner-sheath; BX1, BX3, and BX4. Those that are not fitted; BX2a in the spine and CX1a in the sheath, are very faint knots and as discussed in Section 3.1. The interpretation of these measurements is discussed in Section 4.4.

We also calculated the radio spectral indices between 4.8 and 8.4 GHz for all the radio knots utilizing our multi-frequency 2007 radio data. Due to the low dynamic range of the 22.5 GHz map, we cannot measure fluxes for many of the knots; however, for those which are resolved, the spectral index for 4.8–22.5 GHz, $\alpha_{4.8}^{22.5}$, is consistent with the 4.8–8.4 GHz spectral index ($\alpha_{4.8}^{8.4}$). The errors on these spectral index measurements are dominated by the noise in the images. These are listed in Table 7 with the radio and X-ray flux densities, X-ray photon indices and X-ray/radio ratios, which are discussed in Section 3.7.

3.7. Counterparts

We have identified 13 knots that are detected in both radio and X-ray: A1A and AX1A, A1C and AX1C, A2A and AX2, A3A and AX3, A3B and AX4, A5A and AX5, A6A and AX6, B1A and BX2, B2 and BX4, SJ3 and SJX1B, S1 and SX1A, S2A and SX2A, and S2B and SX2B. Each of the knots in these pairs has the same coordinates with no significant offsets; we do not consider knots with possible offset counterparts as paired, given the discussion of offsets in Hardcastle et al. (2003), who argued that the apparent offsets between the radio and X-ray knots in more distant radio galaxies are a result of an inability to resolve faint-aligned radio-knot counterparts from bright downstream diffuse emission.

With the radio and X-ray data for these knots, we were able to measure the ratio of the 1 keV X-ray flux density and the 8.4 GHz radio flux density, and use the median of these X-ray/radio flux density ratios to determine whether those without detected counterparts are truly without counterparts or whether the counterpart is too faint to be detected. Using the median value of the X-ray/radio flux density ratios, we predicted the flux density of the missing counterparts for the radio-only and X-ray-only knots. The median value of 1.01×10^{-6} is used rather than the mean, as the distribution of these X-ray/radio flux density ratios is not Gaussian. The measured X-ray/radio flux density ratios range from 0.07×10^{-6} to 9.44×10^{-6}. These predicted flux densities assume that all the knots have the same spectrum with consistent X-ray/radio flux density ratios. By comparing these predictions to the measured flux densities, we determined whether the absent counterpart can be detected.

Out of the six radio-only knots, we find that all except two radio knots, A1D and A1E, should have detectable X-ray counterparts using the median X-ray/radio flux density ratio value; however, at the lower limit, only SJ1 should have a detectable X-ray counterpart. Unfortunately, SJ1 is located only 1 arcsec (∼17 pc) from the core, so in the X-ray, the emission from the knot is contaminated by the bright core. In *Chandra* High Resolution Camera observations taken in 1999 (Kraft et al. 2000), SJ1's X-ray counterpart is still unresolved from the nucleus despite the slightly higher spatial resolution. As 7/9 radio knots have detectable but unseen X-ray counterparts when the median ratio is assumed, they probably have steeper spectra than those that have detected counterparts suggesting a genuine difference in their particle acceleration properties.

When we invert this rationale and consider the X-ray-only knots, we find that 9/27 X-ray knots would have detectable radio counterparts at the median X-ray/radio flux density ratio and, as they are not seen, they are likely to have flatter ratios than those that do have detected counterparts. However, at the limits of the range of measured ratios, all these knots are detectable at the lower limit and not detectable at the upper limit.

If we reverse this argument and consider the X-ray/radio flux density ratio values, we would measure if the missing counterpart were at the limit of the noise in the image, we can obtain upper limits on the X-ray/radio flux density ratio for the radio-only knots and lower limits for the X-ray-only knots. In Figure 9, we show histograms of the X-ray/radio flux density ratios for the three populations. As the radio-only and X-ray-only knots give us limits, we find that the peaks of all three groups of knots are consistent, so we cannot rule out a single population; however, we will continue to discuss the knots in three groups and accept that many of the knots may have the same production mechanisms.

Table 7
Spectral Properties of the Radio Knots

Name		Flux Density		S_X/S_R	Radio Spectral Index		$\alpha_{4.8}^{X}$	α_X	N_H
X-ray	Radio	8.4 GHz (mJy)	1 keV (nJy)	($\times 10^{-6}$)	$\alpha_{4.8}^{8.4}$	$\alpha_{4.8}^{22.5}$			($\times 10^{22}$ cm^{-2})
AX1A	A1A	22.89 ± 1.21	10.65 ± 1.64	0.46 ± 0.07	0.89 ± 0.34	0.85 ± 0.21	0.85 ± 0.14	$1.08^{+0.04}_{-0.04}$	0.51 ± 0.02
...	A1B	46.24 ± 1.08	<19.38		0.84 ± 0.18	0.80 ± 0.07			
AX1C	A1C	40.34 ± 2.27	21.43 ± 2.97	0.48 ± 0.09	0.89 ± 0.22	0.79 ± 0.14	0.85 ± 0.23	$1.06^{+0.04}_{-0.04}$	0.52 ± 0.02
...	A1D	8.45 ± 0.77	<3.20		1.56 ± 1.01	0.89 ± 0.41			
...	A1E	9.07 ± 1.00	<1.41		1.66 ± 1.11	1.42 ± 0.88			
AX2	A2A	25.54 ± 1.35	9.29 ± 0.54	0.39 ± 0.04	1.57 ± 0.40	1.16 ± 0.23	0.86 ± 0.08	$0.77^{+0.07}_{-0.06}$	0.55 ± 0.04
AX3	A3A	3.12 ± 0.28	4.02 ± 0.39	1.00 ± 0.49	...	...	0.80 ± 0.14	$0.78^{+0.16}_{-0.15}$	0.40 ± 0.07
AX4	A3B	19.22 ± 1.05	4.98 ± 0.28	0.26 ± 0.04	1.93 ± 0.59	...	0.88 ± 0.08	$0.94^{+0.16}_{-0.15}$	0.45 ± 0.06
...	A4	25.92 ± 2.81	<9.48		1.96 ± 0.49	...			
AX5	A5A	1.64 ± 0.21	6.60 ± 0.39	3.02 ± 7.01	...	...	0.61 ± 0.10	$0.59^{+0.11}_{-0.14}$	0.59 ± 0.07
AX6	A6A	2.41 ± 0.34	9.39 ± 0.35	5.64 ± 2.82	3.91 ± 2.84	...	0.70 ± 0.11	$0.51^{+0.04}_{-0.06}$	0.51 ± 0.05
BX2	B1A	2.23 ± 0.35	19.39 ± 0.97	9.44 ± 5.35	1.89 ± 1.29	...	0.67 ± 0.11	$0.63^{+0.02}_{-0.02}$	0.11 ± 0.01
BX4	B2	4.59 ± 0.46	4.94 ± 0.30	1.80 ± 0.92	4.88 ± 2.82	...	0.77 ± 0.11	$0.91^{+0.06}_{-0.02}$	0.08
...	SJ1	18.69 ± 0.97	<46.79		−0.54 ± 0.06	...			
...	SJ2	3.58 ± 0.84	<19.24		1.86 ± 1.60	...			
SJX1B	SJ3	1.35 ± 0.26	0.99 ± 0.12	0.65 ± 0.44	...	...	0.83 ± 0.19	0.50	0.08
SX1A	S1	9.37 ± 0.78	0.65 ± 0.06	0.07 ± 0.02	2.47 ± 0.84	...	0.96 ± 0.12	$0.48^{+0.12}_{-0.18}$	0.08
SX2A	S2A	1.17 ± 0.86	3.21 ± 0.21	1.78 ± 1.26	...	...	0.77 ± 0.58	$0.64^{+0.07}_{-0.07}$	0.15 ± 0.04
SX2B	S2B	0.43 ± 0.85	1.88 ± 0.26	4.14 ± 7.85	...	...	0.75 ± 2.21	$0.77^{+0.20}_{-0.19}$	0.13 ± 0.06
Inner pc-scale jet		32.13 ± 4.65	7.34 ± 2.41	0.23 ± 0.08	...	...	0.89 ± 0.32	$0.63^{+0.13}_{-0.11}$	0.32 ± 0.07

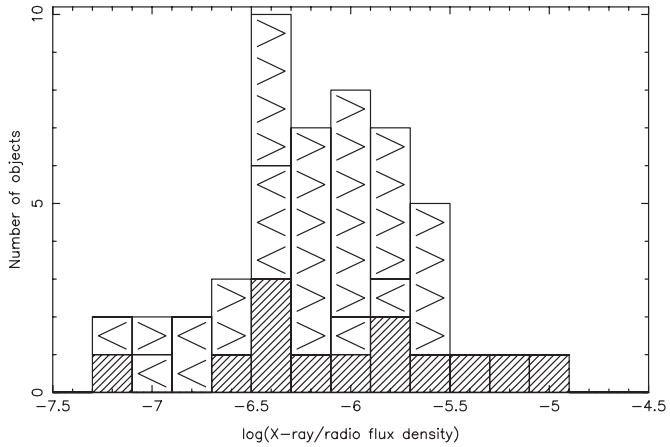

Figure 9. Histogram of the X-ray/radio flux density ratios for the paired knots (hashed region), the lower limits on the X-ray/radio flux density ratio for the X-ray-only knots (>), and the upper limits on the X-ray/radio flux density ratio for the radio-only knots (<) in Cen A.

The properties of these three populations of knots are summarized in Section 3.8; in Section 4, we shall discuss current knot formation and particle acceleration models, and how they explain the differences in the properties of these populations of jet knots.

3.8. Summary of Knot Properties

We have measured the radio and X-ray flux density variability in the knots, the polarization variability, the proper motions and spectral properties of the 19 radio and 40 X-ray knots. Here we summarize the properties of the 13 radio knots with X-ray counterparts, the 6 radio-only knots, and the 27 X-ray-only knots. The following results and groupings are summarized in Table 5.

3.8.1. Knots with Counterparts

Considering the 13 matched knots, we find that only A3B has a well-determined proper motion in the radio at an apparent velocity of $v/c = 0.80^{+0.15}_{-0.02}$. Up until the radio knot A4, the knots with counterparts are likely stationary with low limits and median velocities; however, beyond A4 and in the counterjet, the velocities are inconclusive. These radio knots are generally less compact and fainter and so are more affected by artifacts.

Two knot pairs (A1C/AX1C and B1A/BX2) vary in both radio flux density at 8.4 and 4.8 GHz and X-ray flux density; of these only A1C varies in polarization angle. The increase in radio flux density in A1C is consistent with what was seen by Hardcastle et al. (2003) and similar to the change in X-ray flux density.

None of these matched knots varies only in the X-ray, while two vary only in the 8.4 GHz radio (B2 and S2A); B2 also varies in the degree of polarization. A1A and A3A vary in the 8.4 GHz radio data, but do not pass our requirement for significant variability in our 4.8 GHz data, while S1 varies at both 8.4 GHz and 4.8 GHz. Due to the long intervals in the 4.8 GHz data, we cannot rule out that it is consistent with the 8.4 GHz radio so only use the 4.8 GHz data to determine the spectral indices of the radio knots.

The remaining six pairs of knots vary in neither X-ray nor radio with two showing a change in the polarization; A2A varies in the angle of polarization and A1A varies in angle and degree of polarization. Only two of these knot pairs are completely stable; A5A and SJ3.

3.8.2. Radio-only Knots

There are six radio-only knots but the motions of these are mostly inconclusive with only A1B and A1E having well-established velocities ($v/c = 0.53^{+0.06}_{-0.02}$ and $v/c = 0.34^{+0.22}_{-0.15}$, respectively). The high limits on the remaining velocities cannot rule out that all of the radio-only knots are moving. Three radio-only knots are varying in 8.4 GHz radio flux density, A1B, A1D, and SJ1; SJ1 also varies in 4.8 GHz radio flux density as does A1E. With regard to the polarization, any changes seen in the moving knots are attributed to the motion, so we detect changes in the angle of polarization of two knots (A1D and A4) and SJ1 varies in the degree of polarization.

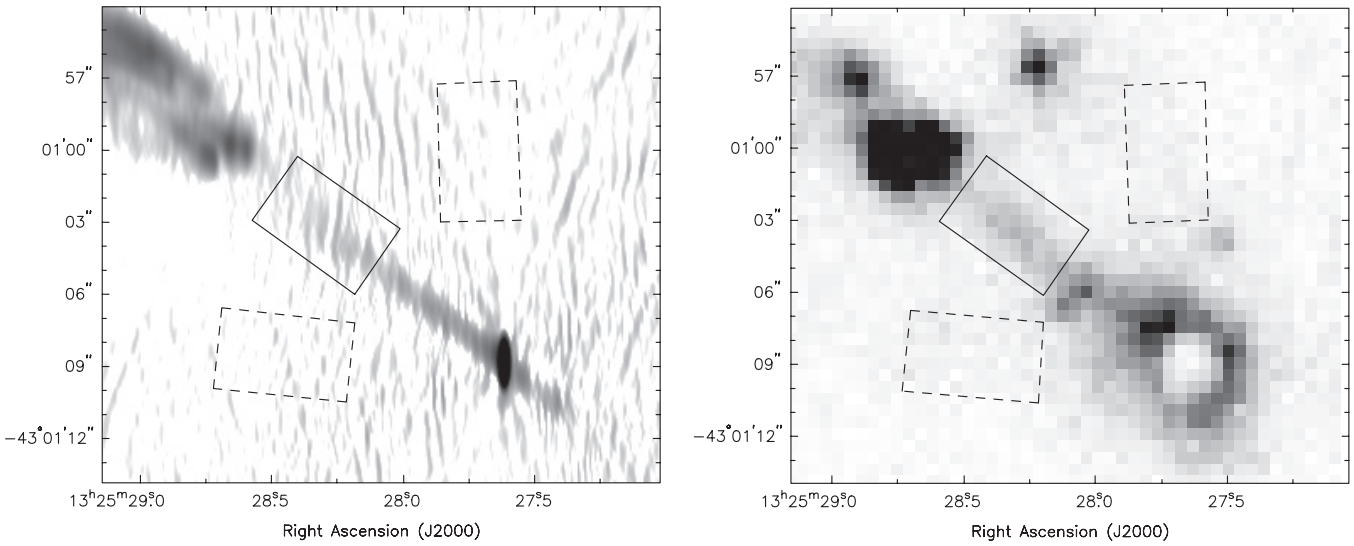

Figure 10. Regions used for the analysis of the hundred-parsec-scale inner jet in Cen A (discussed in Section 3.9) shown against the 2007 8.4 GHz radio data (left) and the combined X-ray data in the energy band 0.4–2.5 keV (right). The source region is shown in the solid line, and the background regions in the dashed line. These regions were chosen to include as emission from only the hundred-parsec-scale inner jet, excluding the emission from the X-ray point sources near the core.

As mentioned in Section 3.7, the broadband spectra of these knots may be steeper than those of the knots with counterparts, suggesting a difference in the particle acceleration between these knots and those with X-ray emission. However, if we consider that they may all be moving, this leaves a group of moving, radio-only knots with half showing signs of radio variability and changes in the polarization.

The radio-only knots with well-established velocities, A1B and A1E, have some degree of radio flux density variability, while the other moving knot, A3B, has a steady radio flux density and has already been described as a group of three subregions with only a diffuse X-ray counterpart. This X-ray emission may not be associated with the moving radio material.

3.8.3. X-ray-only Knots

We detect 27 X-ray knots without radio counterparts and find that the X-ray light curves for five of them show some degree of variability in their X-ray flux densities, including AX2A and SX1, which may be LMXBs (Section 3.1). The vast majority of these knots therefore appear stable and many may have flatter X-ray/radio flux density ratios than those of the knots with counterparts.

We have fitted spectral indices for 14 of these X-ray-only knots and they are all consistent with synchrotron emission lying in the range 0.58–1.40. They are also consistent with those measured for the X-ray knots with radio counterparts (Table 7).

3.9. Inner Hundred-parsec-scale Jet

We detect the inner hundred-parsec-scale jet in both our radio and X-ray data as a very well-collimated feature extending from the core to the A1 base knots, $\sim$250 pc downstream of the nucleus. We used a rectangular region to isolate the emission from this inner jet carefully positioned to include as much jet emission as possible without contamination from the core or the knots; it extends from 6.7 to 12.1 arcsec (114–204 pc) from the core as shown in Figure 10 . The background emission was estimated from two regions, positioned such that they extend radially from the nucleus at the same distances as the jet region, avoiding X-ray point sources.

We measured the X-ray flux densities for each observation and jointly fitted a power law with a spectral index of $0.63^{+0.13}_{-0.11}$ and a Galactic absorption of $0.32^{+0.05}_{-0.02} \times 10^{22}$ cm^{-2} ($\chi^2 = 134.1$ for 133 dof). This spectral index is consistent with the spectral indices of the knots downstream; however, the Galactic absorption is higher in the knots farther downstream than in this hundred-parsec-scale jet, as expected since the jet is located within the optical dust lane. We find that the X-ray to radio spectral index, $\alpha^X_{4.8} = 0.89 \pm 0.08$, is higher but consistent with that of the base knots while the X-ray/radio flux density ratio ($0.23 \pm 0.08 \times 10^{-6}$) is lower than those of the radio knots with X-ray counterparts but higher than the value for diffuse emission in the center jet (Hardcastle et al. 2003; see Section 3.7). We detect no significant variability in the X-ray flux density; the apparent fluctuations appear only minor with no obvious trends. However, the radio 4.8 GHz flux density increased by a factor of 2 from 1991 and shows the first indication of decreasing again in our 2008 data. We are unable to measure the radio spectral index for this region of the jet due to artifacts around the bright core. Although we detect a factor of 2 change in the radio flux density, we cannot make any firm conclusions on this behavior as this section of the jet is greatly affected by artifacts from the core. These results will be discussed in Section 4.5.

4. DISCUSSION

With all of these data, we can begin to shed light on the complicated behavior of the jet: why and where knots are formed, why we can see them, and how they evolve. In this section, we start by examining the many knot formation models and consider if the behavior of any of the knots in Cen A supports them. Not one of these models can explain all of the observed properties of the knots in Cen A; however, some knots behave in a way that can be explained by one model or another. We are particularly interested in seeing if the different populations of knots—those with counterparts, the radio-only and the X-ray-only knots—can all be explained by these models. We then discuss the effect of relativistic beaming on the knot emission, which may explain the observed flux variability, and investigate whether the properties of the knots can be explained by a spine-sheath model of the jet. We also discuss the

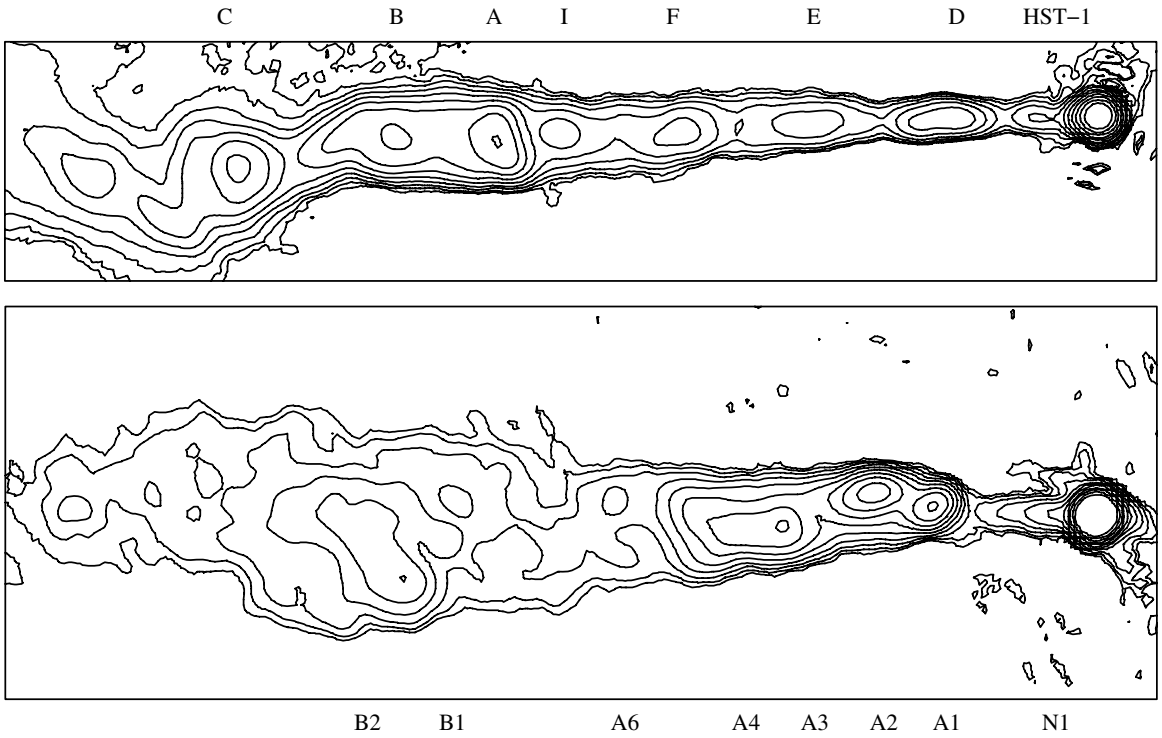

Figure 11. M87 (top) and Cen A (bottom) scaled to a common spatial resolution of 33 pc showing the inner 1.85 kpc of both jets (projected) so that the distances of the knots in each jet can be compared. The Cen A image is our 2002 A+B 8.4 GHz radio data, and the M87 map is at 5 GHz (Hines et al. 1989). The contours are logarithmic increasing by a factor 2 at each step.

hundred-parsec-scale jet comparing it to the knots and to other similar jets.

4.1. Knot Formation Models

To determine whether the current models can explain the knots observed in Cen A, here we compare the observed properties of the knots with the predicted behavior due to changes in the fluid, namely compression or rarefaction, or changes in the particle acceleration due to processes such as reconfinement of the jet, magnetic field reconnection, or collisions with objects such as molecular clouds and high-mass-loss stars.

4.1.1. Adiabatic Compression

If a section of the jet's diffuse material underwent adiabatic compression, the magnetic field, which is frozen into the jet plasma, would increase in strength as would the number density and energies of the emitting particles. This would be reflected in an increase in the flux density and the break frequency of the synchrotron spectrum, so we would observe a flatter X-ray to radio spectrum if compression was responsible for the knots. Hardcastle et al. (2003) calculated the required one-dimensional compression factors, $\mathcal{R}$, from the observed X-ray/radio spectrum using the break frequency ($\nu_b \propto \mathcal{R}^4$ for a tangled field geometry) and considered whether this level of compression, when applied to the surrounding diffuse material, is consistent with the observed emission properties. They found that this level of compression would cause an increase in the radio volume emissivity of the diffuse material by a factor of $\sim 10^{11}$ compared to the observed factor of ~ 2, effectively ruling out compression as a creation model for the X-ray-only knots in Cen A. Compression in more than one dimension may reduce the effect to a change in break frequency of $\nu_b \propto \mathcal{R}^2$; however, the change in volume emissivity is still much higher than the observed factor. Lesser amounts of compression may still explain the radio-only knots where the X-ray/radio flux density ratio of the diffuse material is suppressed, resulting in a X-ray counterpart too faint to be detected above the diffuse emission, but they cannot explain any knot with an X-ray counterpart. In what follows, we therefore consider only particle acceleration models as causes for radio knots with X-ray counterparts and X-ray-only knots in Cen A. It seems very likely that more than one of these particle acceleration processes is responsible; here we examine in detail the predictions of the models and the observed behavior of the knots to identify those models which are dominant in the jet.

4.1.2. Impulsive Particle Acceleration

If the knots seen in Cen A are the result of impulsive particle acceleration across the entire knot region, due to a short-lived processes such as small-scale magnetic field reconnection, they would fade due to synchrotron losses while others would presumably appear in order to maintain a steady state. Using the equipartition value of the magnetic field strength in the A1A knot (Section 3.2), we would expect a complete change in the appearance of the 1 keV X-ray jet emission in ∼6 years; this is not seen. The X-ray synchrotron lifetimes of some of the knots that are resolved in the radio are shown in Table 4. Consequently, the particle acceleration processes must be in general long-lived.

The knot HST-1 in M87 may be an impulsive event as it flared and faded to approximately its original flux in a decade. The observed fading is consistent with synchrotron losses; in addition to a general decrease in all frequencies (X-ray, UV, and radio) consistent with changes in the beaming factor, the X-ray falls off faster than the UV or radio (Harris et al. 2009). However, no knot in Cen A appears to behave like HST-1; the

largest increase in flux is only a factor of 3 over the last 16 years (SJ1), much slower than the flaring of HST-1, and it has not yet begun to fade. SJ1 is better described by a collision model (Section 4.1.5).

4.1.3. Collisions

A collision between the jet and an obstacle (Blandford & Königl 1979) would result in a local shock complex and is therefore commonly invoked to explain jet knots. In this scenario, during the initial interaction, we would see a steady increase in the luminosity of the knot relative to the diffuse background. This is a fast process relative to the lifetime of the knots, but for plausible obstacle sizes and speeds it is much longer than the period of our observations and would therefore only be seen as a slight increase in flux. Once the obstacle is firmly in the path of the jet, we expect to see a prolonged period of stable particle acceleration. Eventually, the obstacle may be annihilated by the constant impact from the jet fluid; it could move transversely out of the jet, continuing on its original path; or it could be carried along the jet, which would cause a reduction in the shock strength as the obstacle accelerates. All these would result in a gradual decrease in the flux and, eventually, to the complete disappearance of the knot.

In Cen A's jet, we can therefore expect to see a range of behaviors for local shocks in the jet, but the vast majority of knots in this model are expected to be in a phase of stability with X-ray and radio emission of a constant flux. The knots A1A/AX1A and A1C/AX1C are possibly local shocks due in some part to the reconfinement of the jet (see Section 4.1.4); however, there are many other instances where there is an X-ray compact source associated with a stationary compact radio knot: A2A/AX2, A5A/AX5, B1A/BX2, and B2/BX4 in the jet, and SJ3/SJX1b, S2A/SX2A and S2B/SX2B in the counterjet. There are some slight changes in the X-ray, radio or polarization in these systems, but these are not steady, broadband increases or decreases which could be attributed to beaming (Section 4.3). Their variability may be described as short-term flaring and may be due to the evolution of the interaction between the jet and the obstacle, to fluctuations in the jet's fluid flow, or to their shock being curved, which would be naturally unsteady under small perturbations of the driving flow.

The majority of the X-ray knots have no detected radio counterparts and only five of these X-ray-only knots have variability detected in the X-ray flux density, of which two are probably LMXBs (Section 3.1). Of the three probable jet knots, FX1A has a significant flaring event (X-ray increases by a factor of 2 in the 2002 observation), EX1 shows evidence of a steady decrease in the 2007 VLP observations, which is consistent with predictions of synchrotron losses, and GX5, a very faint knot, is only detected in 3 of the 10 observations so that we cannot characterize its variability in detail. Despite these exceptions, the vast majority of these stationary, X-ray-only, compact knots are consistent with a period of stability in the shock model where the radio counterpart is too faint to be detected in our data; the range of X-ray/radio ratios we have measured means we cannot dismiss the possibility of faint radio counterparts, and in fact there is diffuse material emitting in the radio at many of these positions.

It is still possible that the X-ray-only knots are a separate population of knots that have flatter spectra than the radio knots with X-ray counterparts; however, these knots and those with detected counterparts are consistent with collisions and shock models although we do not see any knots at a stage where the knots are fading away, which would be a very short period in the lifetime of the knot compared to their stable stage. We do see one knot, AX2A, appearing in the X-ray during our 2007, 6×100 ks observations but we do not observe a gradual brightening as there is a four-year gap in the observations prior to the 2007 observations when this may have occurred, so we cannot say for certain whether this is a new knot or a LMXB (Section 3.1).

The radio-only stationary knots may be explained in this scenario by a weaker shock such as would occur if the obstacle is moving downstream. As the obstacle is sped up to match the fluid flow, the shock would weaken until it was too weak to accelerate particles to X-ray emitting energies. In this model, the ratio of the numbers of radio and X-ray knots would be related to their respective lifetimes, but as the lifetime of the knots also depends on the birth rates, the times taken for the knots to move along, through or out of the jet, and the obstacle ablation or acceleration timescales, the relationship would not be a simple one. This model explains stationary and very slow moving knots but those moving at close to the mean jet speed ($v/c \sim 0.5$) cannot be explained by weak shocks, and the limits on the proper motions of the radio-only knots suggest that many knots may not be consistent with this model. A1D is an example of this with an upper limit speed of $0.58c$. Other models for the radio-only knots are discussed further in Section 4.1.5.

Recent 2.3 GHz Very Long Baseline Interferometry (VLBI) observations by Tingay & Lenc (2009) of the bright A-group knots do not detect our moving radio knots, A1B and A1E, or A1D while the compact cores of A1A, A1C and A2A are all resolved. These results strongly support a collision model for, at least, the stationary radio knots with X-ray counterparts, and also argue that there is an intrinsic difference between the stationary and moving knots. If the stationary knots were due to collisions with an obstacle, we would expect to detect a compact region where the interaction is occurring; whereas if the moving knots were due to a non-localized process such as compression of the fluid flow, we would not expect to detect a compact central region in the knot.

If we consider the limits on the proper motions of the stationary knots (A1A; $v/c < 0.05$, A1C; $v/c < 0.14$ and A2A; $v/c < 0.24$) it is reasonable to consider A3A, with a limit of $v/c < 0.05$, to also be stationary and therefore we can predict that in principle it should be detectable with VLBI. The limits on the other knots are all significantly higher and in two cases, unconfined (A4 and B2) so if these knots have compact cores that can be detected with VLBI they could be independently identified as either moving or stationary knots. This is particularly interesting in the case of SJ1 as it has a measured velocity of $v/c = 0.42^{+0.39}_{-0.27}$, but this apparent velocity is due to the effect of artifacts on the observed shape of the knot. We cannot resolve a X-ray counterpart due to its proximity to the core (0.95 arcsec = 17 pc), so detecting a compact peak in the radio with VLBI might give us an independent method of constraining its motion and therefore the reason for its development.

Tingay & Lenc (2009) also detect sub-structure in the knots A1A and possibly A2A. (The larger-scale structure of these knots is not detected by the VLBI observations due to the lack of short baselines.) If we consider A1A, which Tingay & Lenc (2009) divide into two compact sources A1Aa and A1Ab, we find that Tingay & Lenc (2009) only detect approximately half of the flux at 2.3 GHz (from both of these substructures) that we

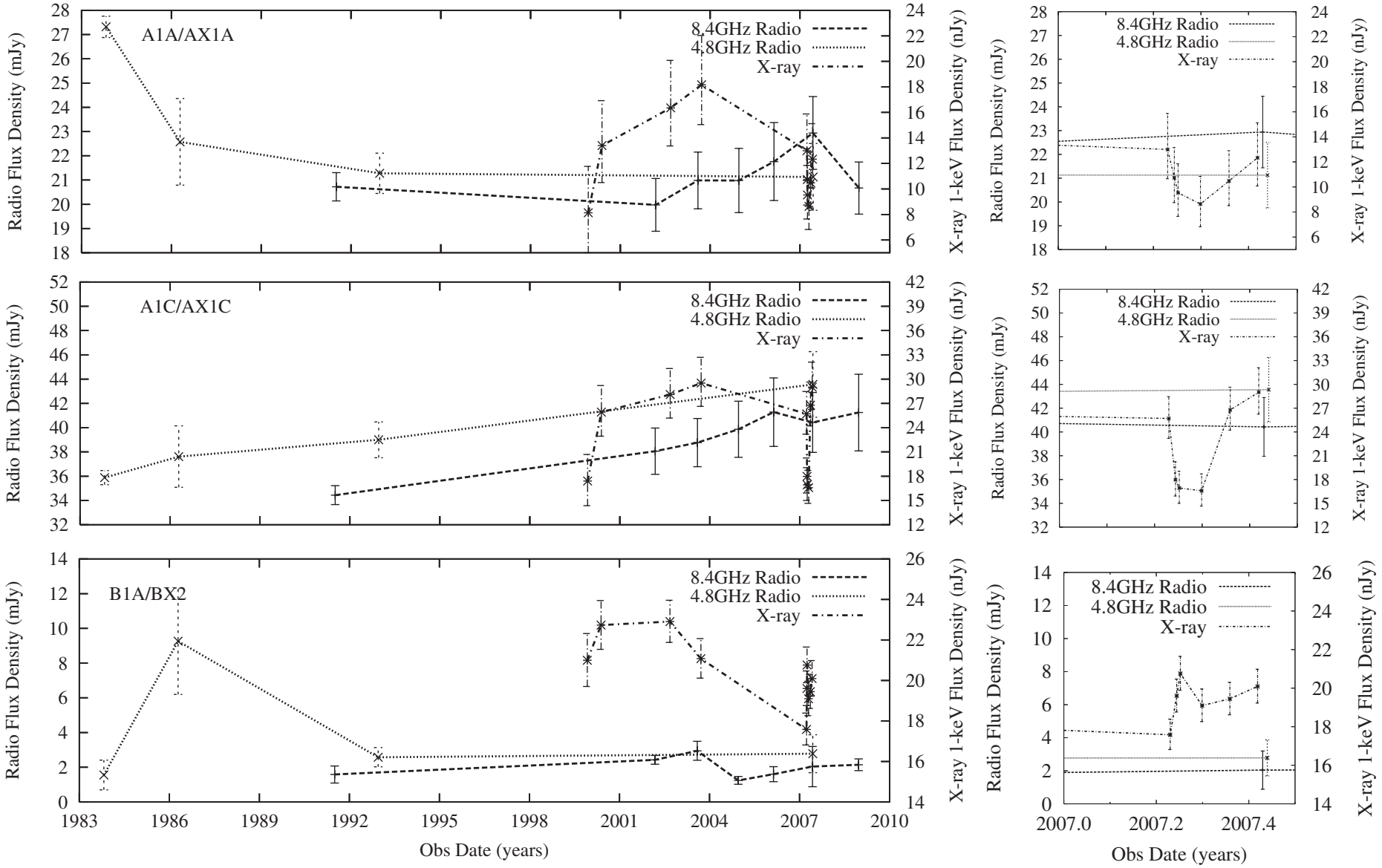

Figure 12. X-ray and 8.4 GHz radio light curves for the radio knots in Cen A, which show some degree of radio or X-ray variability AND have X-ray counterparts; A1C (top panel), B1A, (middle panel), and B2 (bottom panel). The right-hand images are cropped to highlight changes in the X-ray flux density during the *Chandra* VLP observations.

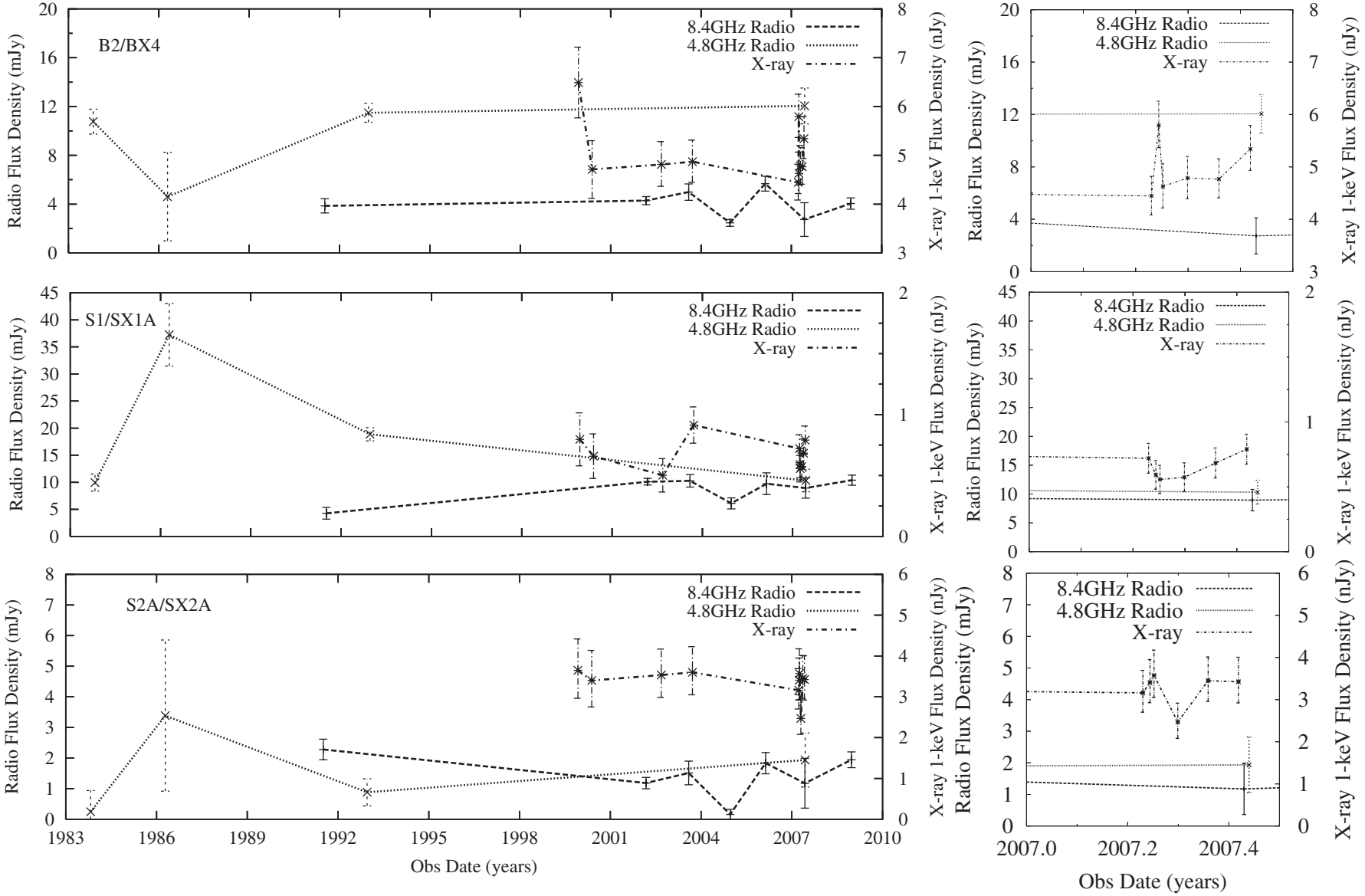

Figure 13. X-ray and 8.4 GHz radio light curves for the radio knots in Cen A, which show some degree of radio or X-ray variability AND have X-ray counterparts; S1 (top panel), S2A (middle panel), and S2B (bottom panel). The right-hand images are cropped to highlight changes in the X-ray flux density during the *Chandra* VLP observations.

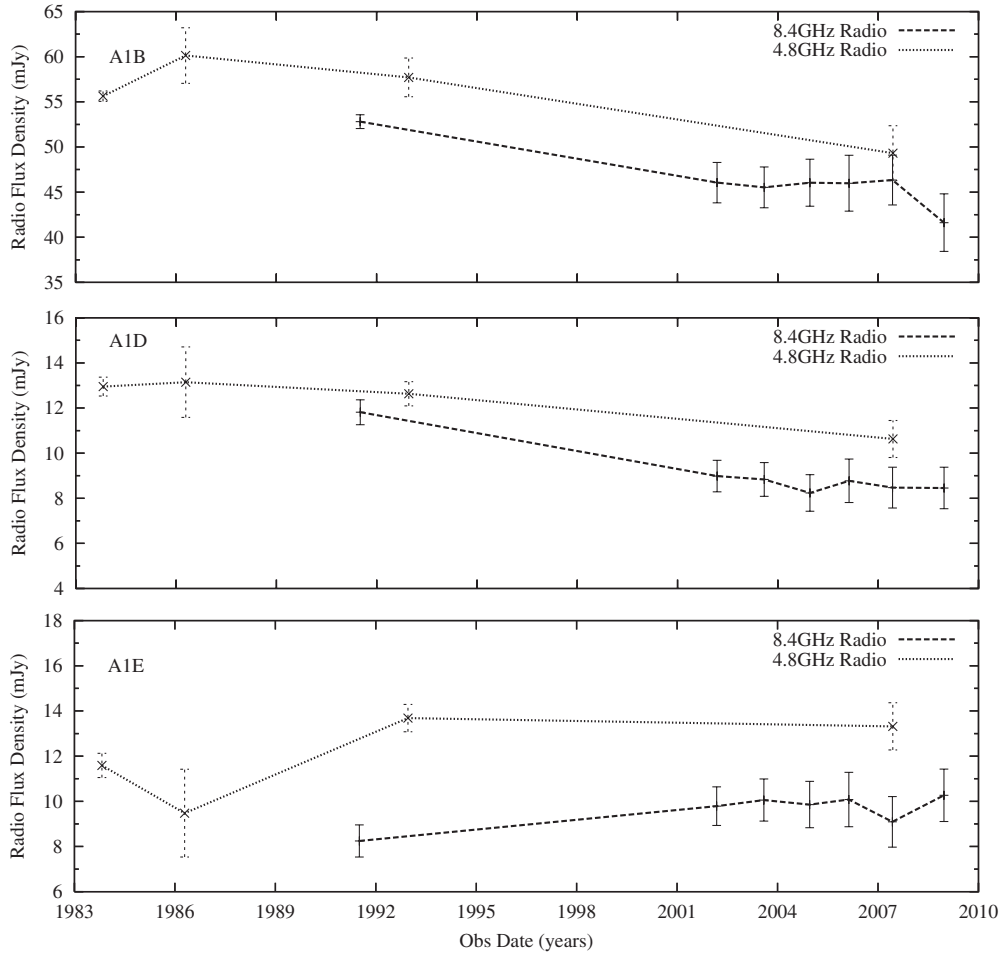

Figure 14. 8.4 GHz and 4.8 GHz radio light curves for the radio-only knots in Cen A; A1B (top panel), A1D (middle panel), and A1E (bottom panel).

would expect based on our observations and assuming a power-law spectrum. We must assume that the remaining half of the emission is coming from more diffuse material on the scale of 0.1–0.2 arcsec. However, the observations of a compact core reduce the possible size of the obstacle to an area comparable to the size of the region detected (0.5–2.5 pc), which suggests an obstacle such as O/B stars, which are much more common, rather than more extreme systems such as Wolf–Rayet stars as suggested by Hardcastle et al. (2003).

As discussed in Section 3, we find that many of the X-ray knots with radio counterparts, and all of the radio-only knots, lie within the inner arcminute (∼1 kpc), while beyond this, we find a complete absence of compact radio knots, even though there is diffuse radio emission extending to the north inner lobe at ∼190 arcsec. It is at ∼1 arcmin that we also detect a change in the absorbing column as the jet emerges from the dust lane. Given the constraints on the geometry of the dust features seen in emission at 8 μm with *Spitzer* IRAC (Quillen et al 2006, 2008), it seems unlikely that the jet is interacting with the dust disk directly beyond the A1 group of knots. However, it remains plausible that there are a greater number of knots in this inner region due to collisions with high-mass-loss stars or clumps of cold gas, both of which will be more common in the central regions of the galaxy. If we consider the distribution of stars in Cen A (van den Bergh 1976; Mellier & Mathez 1987) and compare this with the decreasing number of knots with distance from the core, we find that the number of stars per unit length in the jet steadily increases with distance from the nucleus. This argues that the obstacles are not distributed like normal stars in the galaxy, but does not rule out the model in which the obstacles are high-mass-loss stars or gas clouds associated with the central regions of the galaxy.

Farther out, we see a decrease in the spatial density of knots which is consistent with a predominantly diffuse particle acceleration mechanism and at ∼190 arcsec the environment may change again, as the radio emission expands into a lobe and there is an X-ray surface brightness discontinuity (Kraft et al. 2008).

We conclude that the majority of knots in the jet of Cen A are due to the interaction between the jet and an obstacle, including knots with no detected X-ray or radio counterparts, the exceptions being those radio-only knots which are moving (Section 4.1.5); however, this assumes that the missing counterparts exist below the noise level. If there are really no counterparts, we require another model to explain the existence of X-ray-only knots.

4.1.4. Reconfinement of the Jet

It has been suggested (e.g., Sanders 1983) that where the jet moves from a well-collimated hundred-parsec-scale jet to a complex, knotty kpc-scale jet, the supersonic fluid encounters a less dense environment. It expands into this ambient material and is therefore likely to cause a reconfinement shock near the boundary of the jet. This could also be the case if there is a change in the internal pressure or state of the gas, or because of a change in the external sound speed or density with no change in the external pressure, which could occur if the jet is within a relativistic bubble.

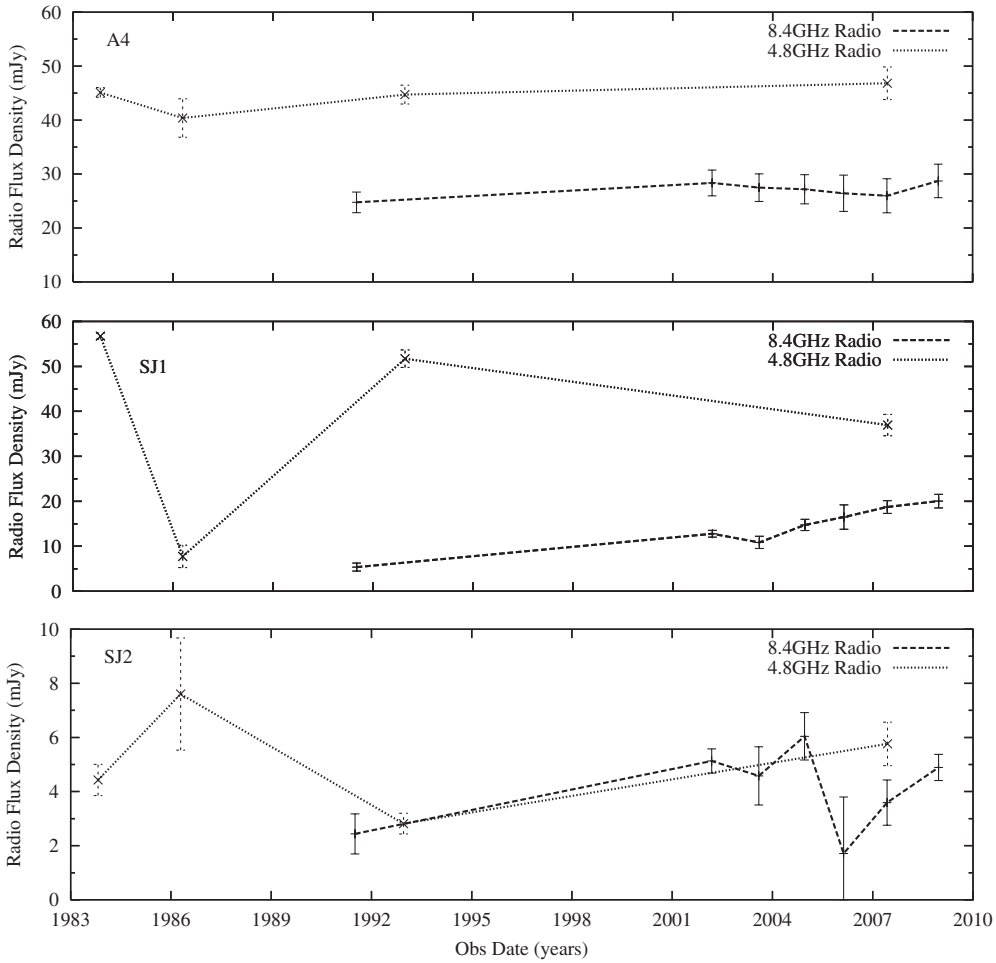

Figure 15. 8.4 GHz and 4.8 GHz radio light curves for the radio-only knots in Cen A; A4 (top panel), SJ1 (middle panel), and SJ2 (bottom panel).

At ∼250 pc, the inner jet of Cen A expands from a well-collimated beam to a diffuse cone of material (Figure 11). This is indicative of a change in the ambient pressure which would be consistent with the conditions for a reconfinement shock. The base knots A1A/AX1A and A1C/AX1C are therefore prime candidates for reconfinement shocks. They are also stationary in the jet, and A1C is evolving downstream consistent with this model. Unfortunately, the presence of the moving knot, A1B, between two base knots is difficult to explain in a simple reconfinement model; it would require a unstable knot complex, possibly ringed, with a shock region that could have been disrupted by A1B as it moves along the jet.

The knot HST-1 in M87 has also been investigated in terms of a reconfinement shock model by Stawarz et al. (2006) and has many traits similar to A1A and A1C. It is believed that the stationary, compact, variable and overpressured flaring region is located immediately downstream of the point where the reconfinement shock reaches the jet axis. Stawarz et al. (2006) also associate the downstream, superluminal features of HST-1 with a diverging reflected shock. If we compare this to Cen A's A1 grouping, then A1A and A1C are consistent with the flaring region of HST-1 and the fainter downstream components A1D and A1E, which are moving down the jet, can be compared to the reflection components.

To summarize, the location of these knots at the point where the jet widens and the fact that, collectively, they span the width of the jet are in favor of a reconfinement shock model; however, the fact that there are two of them and that A1B is apparently moving between them makes this model harder to accept.

4.1.5. Moving Knots

The moving radio knots fit into none of the models discussed previously (see Section 4.1.3) as all these models describe a situation in which the fluid undergoes a change at a stationary point in the jet. We have also to consider that there are no compact X-ray counterparts to the moving radio knots, A1B and A1E, as well as the diffuse radio emission downstream of A2A; A2B ($v/c = 0.57$), A2C ($v/c = 0.25$) and A2D ($v/c = 0.46$). The remaining moving knot, A3B, is associated with a clumpy region in the radio jet rather than a single compact radio knot and has X-ray emission associated with it, although this could be a projection effect or emission from a nearby stationary X-ray knot unrelated to the radio knot. We must also note that all of the radio-only knots have either well-established or inconclusive proper motions so it may be that all of the radio-only knots are moving.

Knots that are moving at speeds comparable to the bulk jet flow speed cannot be due to collisions with a stationary or slow-moving obstacle, and, as we have argued above (Section 4.1.3), there is independent evidence from VLBI observations that there is an intrinsic difference between the moving and stationary knots in the A group. To describe the moving knots we require a scenario in which the jet undergoes a change resulting in a knot of either higher particle density, higher particle energy, or higher magnetic field, which moves freely along the jet with the

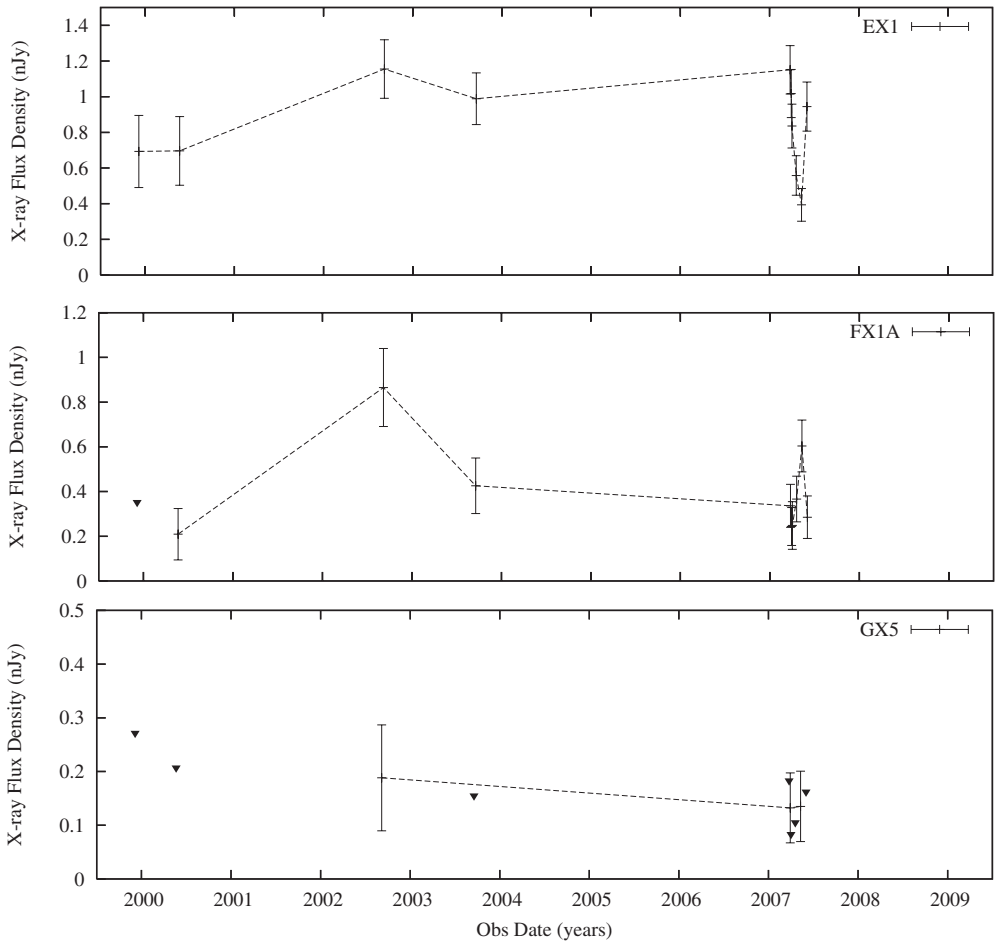

Figure 16. X-ray light curves for the X-ray-only knots in Cen A, which show signs of variability; AX2A (top left), EX1 (top right), FX1A (bottom left), and GX5 (bottom right).

fluid flow. This would be provided by moderate compression of the jet fluid, as discussed in Section 4.1.1.

Information on X-ray motions of the other knots in the jet will be invaluable to this problem as the radio-only moving knots may not be as different as this work suggests, but X-ray proper motions will not be available for some time. Our current data span a sufficient time frame for motions to be detected; however, the signal to noise of the earlier observations is not good enough to accurately measure the position of the knots, so that our *Chandra* data do not provide useful constraints.

4.2. Particle Acceleration Efficiency

In models in which the X-ray emission from the knots is synchrotron emission produced as a result of the interaction between the jet and an obstacle, the X-ray luminosity places some constraints on the efficiency of high-energy particle acceleration. Using the constraints on the knot sizes provided by the VLBI observations (4.1.3), we can calculate the fraction of the jet power intercepted by the knots. Some fraction of this (which cannot exceed 100%) goes to power the emission at X-ray and other bands. If we assume that the knots are in a steady state and that the incident energy produces electrons with a power-law energy spectrum that balances the radiative losses, then we can form an inequality: the ratio of the energy in the X-ray-emitting electrons to that in the whole electron population must be greater than the ratio of the energy emitted in the X-rays to the fraction of jet energy intercepted by the knot. The unrealistic assumption of 100% efficient energy transfer of the absorbed jet energy to relativistic electrons, we find that the electron energy spectrum has an index, $p \leqslant 2.44$, when we consider the lowest energy electrons to have $\gamma = 1$. If we assume that the energy transfer to the electrons is 10% efficient, then the minimum index decreases, $p \leqslant 2.27$, and at 1% the spectrum is constrained to have $p \leqslant 2.06$. However, if the minimum γ is increased to $\gamma = 100$, these indices steepen so, for example, 1% efficient energy transfer has a minimum index of $p \leqslant 2.13$. These calculations use the cross section and X-ray emission of the knot AX1A as its size is well constrained (Tingay & Lenc 2009). These minimum indices put some constraints on the nature of the particle acceleration in the jet; we note that $p > 2.0$, the value expected for standard acceleration at a non-relativistic strong shock, is possible unless the efficiency of energy transfer to the electron population falls below ∼1%.

4.3. Beaming

If there are changes in the beaming factor in the knots, due to a change in the velocity or direction of the fluid flow, we would observe in-step changes in the X-ray and radio flux densities, assuming all the emission is synchrotron, as beaming to first order is independent of frequency. This may occur in stationary or moving knots as the movement of the fluid through the knot is responsible for changes in the beaming factor, not the motion of the knot itself. Although the flaring of HST-1 may be explained as a reconfinement shock or the result of impulsive particle acceleration, it fades in a manner best described by

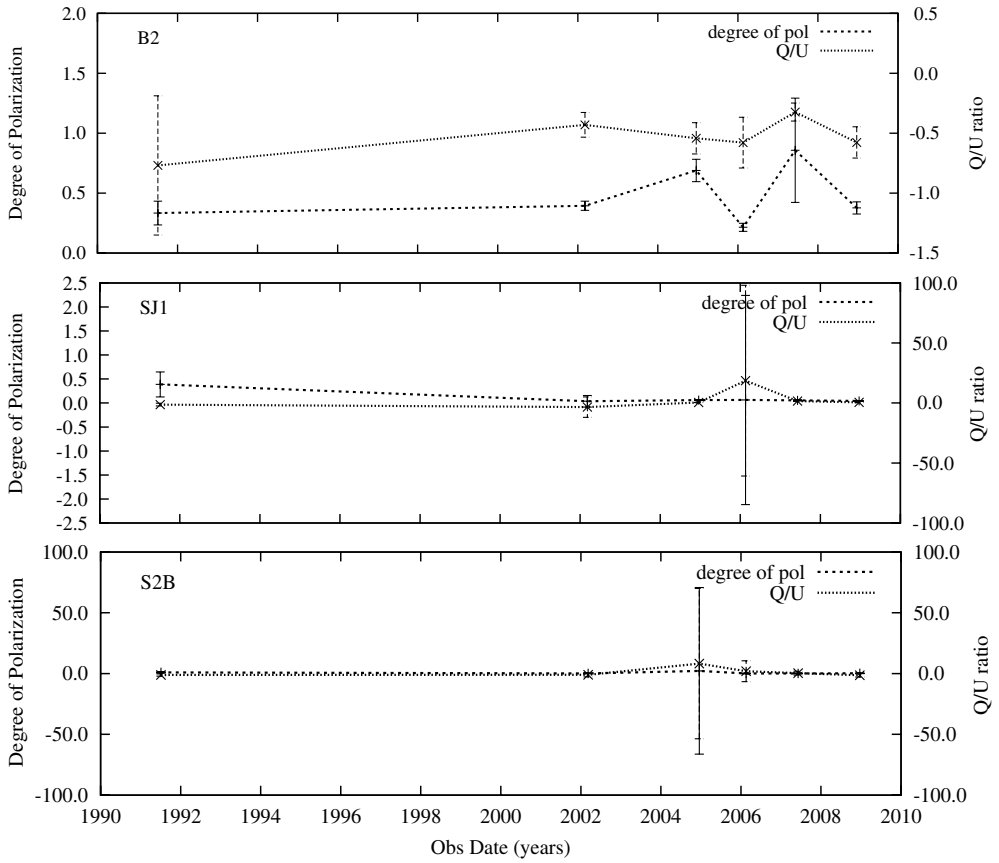

Figure 17. Plots for the radio knots in Cen A, which show significant variability in the degree of polarization only with the degree of polarization (dotted lines) and the angle of polarization (dashed lines): B2 (top panel), SJ1 (middle panel), and S2B (bottom panel).

beaming combined with synchrotron losses (Harris et al. 2009); the emission fades slowly in all frequencies, but appears to drop off faster in the X-ray compared to the UV and radio. Compared to the factor 50 increase in X-ray emission of M87's HST-1, we observe no flaring events of similar intensity in either our radio or X-ray data. The largest increase we observe is in the radio knot SJ1, which increases in radio emission by a factor of 3.5 over the last 17 years. This is the only knot showing variability in the inner hundred-parsec-scale jet region suggesting that it has different physics from the knots farther down the jet and it is better described by a collision and shock model.

Smaller increases are seen in other stationary radio knots, increasing in step in the radio and X-ray although only A1C/AX1C shows a significant change in both. In the radio, A1C increases steadily while in the X-ray we see short-term variability with a dip in the flux density in the middle of 2007 (Figure 15). This is consistent with the short-term variability observed in HST-1, which also show slight dips in the X-ray flux density during an overall increase. The knots A1A/AX1A and S1/SX1A also fit these conditions; however, the subtle increase in flux (∼10%) is below the significance limit described in Section 3.4.

We conclude that although we see in-step changes in the radio and X-ray flux densities in several of the knots, beaming is not the dominant effect as other mechanisms can explain the observed behaviors.

4.4. Spine–Sheath Model

Current models of FRI jets (Laing & Bridle 2002) propose that the jets have a non-uniform radial velocity profile in which the speed decreases with increasing radius. Because of early polarization results that seemed to point to a two-fluid structure, this is often discussed in the literature in terms of a fast-moving "spine" and slower "sheath" of the jet. The almost entirely parallel magnetic field seen in this work and in polarization maps by Hardcastle et al. (2003) provides no evidence in itself either for or against "spine–sheath" models, since modern versions of models with velocity structure do not predict a transition to a central perpendicular field in all cases. Some evidence for models with velocity structure might be provided by the observed localized edge brightening in the diffuse material (Kataoka et al. 2006), if this is predominantly due to variations in the Doppler enhancement of different layers of the jet material. However, this limb brightening is not seen along the entire jet; where it is seen, it lies downstream of a compact knot and could be described as a knot tail. Similar structures are seen behind many of the knots, for example A2A, and are consistent with a shock model with downstream advection Hardcastle et al. (2003). Kataoka et al. (2006) also suggested that at the edges there is a slight hardening of the X-ray emission suggesting the spectrum changes.

To investigate if this is seen in our deeper X-ray data, Worrall et al. (2008) fitted a joint spectrum to all the X-ray knots that reside in the "inner-spine" and "inner-sheath" regions (at a distance of 21–66 arcsec from the core with P.A.s of 51°.2 and –57°.8 for the spine, and 49°,–51°.2, and 57°.8–60° for the sheath[13]). As described in Section 4.4, we have spectral fits for six of the seven X-ray knots in the inner-spine and three of the five X-ray knots in the inner-sheath regions defined

[13] Worrall et al. (2008) defined these pie sections from a base position of 13:25:26.98 −43:01:14.06 (not the core).

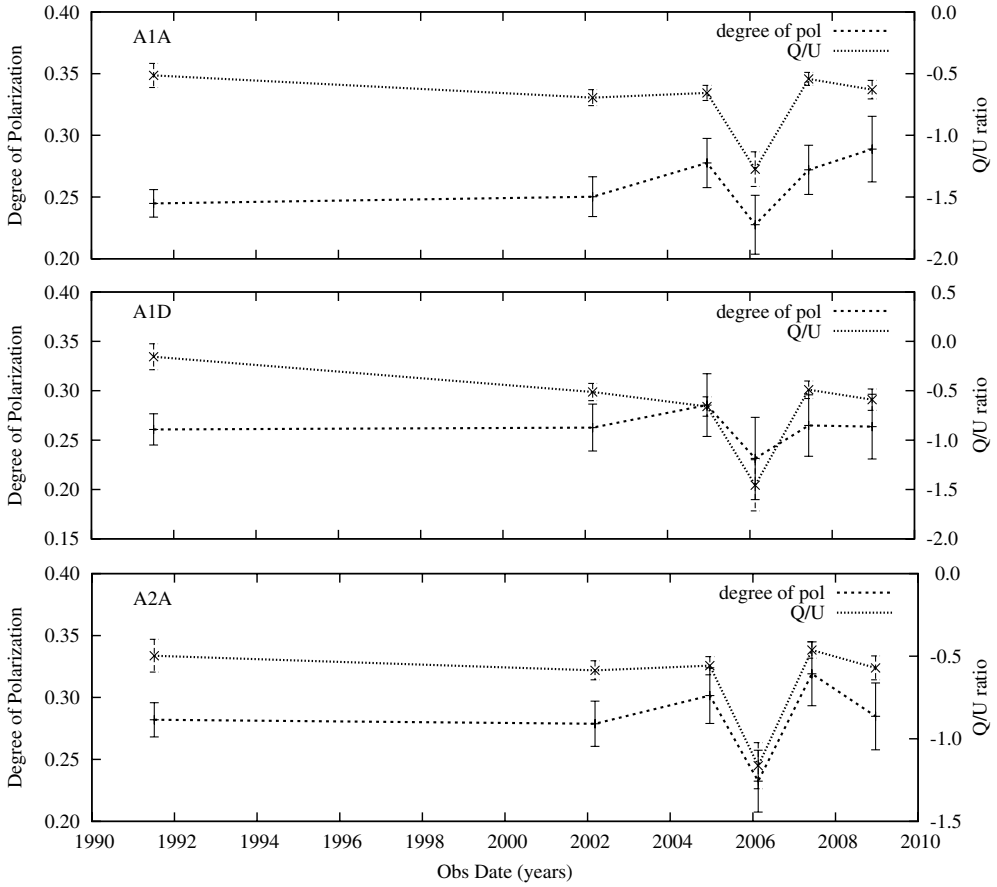

Figure 18. Plots for the stationary radio knots in Cen A, which show significant variability in the angle of polarization only with the degree of polarization (dotted lines) and the angle of polarization (dashed lines): A1A (top panel), A1C (middle panel), and A2A (bottom panel).

by Worrall et al. (2008). The weighted mean of the spectral indices we measure for the X-ray knots in these regions are $\alpha_{\rm spine} = 0.62 \pm 0.01$ and $\alpha_{\rm sheath} = 0.89 \pm 0.05$, respectively, which are consistent with the results of Worrall et al. but not with each other. On closer inspection of the individual knot spectral indices, we find that the inner-spine spectral index is dominated by the bright X-ray knot BX2 ($\alpha_X = 0.67 \pm 0.11$). Given the small number statistics and the dominance of individual knots, it is difficult to draw conclusions about the behavior of either knot population.

As discussed in Section 3.3, we see no dependence of the velocities on the angular position of the knots, nor on the distance of the knots from the core, although our sample is too small for a statistical analysis. We have considered the directions of motion and find that they are consistent with following the fluid flow, appearing to move toward the downstream regions of bright material. The directions of motion are not consistent with moving exactly parallel to the jet axis but we argue that the ridge line through the jet is not at a constant positional angle and that the fluid flow is complicated and not a simple laminar flow directed away from the core. We therefore cannot comment further on the possibility of a faster moving spine in the jet of Cen A nor on the possible migration of the knots toward or away from the jet axis.

4.5. Inner Hundred-parsec-scale Jet

We found that the spectrum of the inner hundred-parsec-scale jet of Cen A is flatter in the X-ray than the base knots and the diffuse material (Hardcastle et al. 2003) but consistent in the radio to X-ray spectral index. These measurements are also consistent with the values for knots farther along the jet. The X-ray/radio flux density ratio is lower for the inner hundred-parsec-scale jet than for any of the knots, except S1/SX1A; however, it is higher than the X-ray/radio flux density ratio of the diffuse material farther down the jet suggesting that the inner jet is more efficient at making X-rays for a given amount of radio than the diffuse emission farther up the jet. This is consistent with what is seen in other FR I jets such as that in 3C 66B (Hardcastle et al. 2001).

5. SUMMARY AND CONCLUSIONS

Our results can be summarized as follows.

1. We rule out impulsive particle acceleration in the knots of Cen A as we detect no extreme variability in the X-ray knots, in contrast to what is seen in knot HST-1 in M87. We see essentially the same distribution of X-ray knots in our most recent observation as was seen in the earliest *Chandra* observations in 1999. This would not be the case if the knots were impulsive as they would fade due to synchrotron losses indicating long-lived particle acceleration in the knots of Cen A.
2. For those radio knots with X-ray counterparts, the most likely formation mechanism is a collision between the jet and an obstacle, resulting in a local shock. We see no significant variability in many of these knots, suggesting a long-lived, stable stage of particle acceleration during the interaction between the jet and the obstacle.
3. The formation of knots at the point where the inner hundred-parsec-scale jet broadens abruptly suggests that these base

knots (A1A and A1C) may be reconfinement shocks; however, this is complicated by the presence of a radio-only knot (A1B) moving downstream between the possible confinement-shock knots.

4. We detect a factor of 3 increase in radio flux density of the counterjet knot SJ1. This knot lies only 17 pc from the nucleus so is unresolved in the X-ray; however, it was still increasing in flux in the most recent observation (2008 December) so we plan to continue to monitor its radio behavior with the VLA.
5. We detect proper motions in three of our radio knots; two of which have no compact X-ray counterparts and a third which has only diffuse X-ray emission associated with it. Studies of the distribution of the moving knots are inconclusive due to the low number of well-established proper motions, however, that the direction of motion of the knots may not be directly parallel to the jet axis which appears to varies along the jet. Their motions are all downstream and they show no dependence on the position of the knot within the jet.

The most likely cause of knots in the jet is collisions; if the X-ray-only knots have faint radio counterparts and the radio-only knots are seen only during the latter stages of the collision when the interaction is weaker, then only the moving knots are a separate population. These may include all the radio-only knots but our proper motion measurements are inconclusive for many of these. We argue that these moving knots are due to compressions in the fluid flow that do not result in particle acceleration to X-ray emitting energies. It is possible, however, that the X-ray-only knots are also a separate population with flatter X-ray to radio spectra than those with counterparts, in which case we currently have no model for their formation.

Compared to other FR I jets, Cen A is atypical, with an obscuring dust lane extending out to 1 kpc from the core which greatly affect the jet and its knots. Other galaxies where dust has been detected, such as 3C31 and 3C449, have much smaller disks, which cannot affect even the innermost regions of the observed X-ray jet. If we can attribute the knot dominated particle acceleration of the inner kpc to the presence of this disk then we can postulate that the X-ray jet emission seen in other FR I galaxies should be comparable to the dominant diffuse particle acceleration that dominates farther out in the Cen A jet. We would then predict that knot-dominated structure will not be seen in other FR I galaxies.

We gratefully acknowledge financial support for this work from the STFC (research studentship for J.L.G.), the Royal Society (research fellowship for M.J.H.), and NASA (grant GO7-8105X to R.P.K.). The National Radio Astronomy Observatory is a facility of the National Science Foundation operated under cooperative agreement by Associated Universities, Inc. We acknowledge helpful comments from an anonymous referee.

Facilities: CXO (ACIS), VLA

APPENDIX

FLUX VARIABILITY PLOTS

Figures 12 and 13 show the light curves for those radio knots with X-ray counterparts; Figures 14 and 15 show the radio and X-ray light curves for the radio-only knots. Figure 16 shows the X-ray only knots. Figure 17 shows those knots with changes in the degree of polarization; Figure 18 shows those with changes in the angle of polarization.

REFERENCES

Bicknell, G. V. 1984, ApJ, 286, 68
Biretta, J. A., Sparks, W. B., & Macchetto, F. 1999, ApJ, 520, 621
Blakeslee, et al. 2009, ApJ, 694, 556
Blandford, R. D., & Königl, 1979, ApJ, 20, L15
Brookes, M. H., Lawrance, C. R., Stern, D., & Werner, M. 2006, ApJ, 646, L41
Cheung, C. C., Harris, D. E., & Stawarz, Ł. 2007, ApJ, 663, L65
Clarke, D. A., Burns, J. O., & Norman, M. L. 1992, ApJ, 395, 444
Croston, J. H., Hardcastle, M. J., Birkinshaw, M., Worrall, D. M., & Laing, R. A. 2008, MNRAS, 386, 1709
Croston, J. H., et al. 2009, MNRAS, 395, 1999
Fabbiano, G. 2006, ARA&A, 44, 323
Fanaroff, B. L., & Riley, J. M. 1974, MNRAS, 167, 31
Feigelson, E. D., Schreier, E. J., Delvaille, J. P., Giacconi, R., Grindlay, J. E., & Lightman, A. P. 1981, ApJ, 251, 31
Ferrarese, L., Mould, J. R., Stetson, P. B., Tonry, J. L., Blakeslee, J. P., & Ajhar, E. A. 2007, ApJ, 654, 186
Hardcastle, M. J., Birkinshaw, M., & Worrall, D. M. 2001, MNRAS, 326, 1499
Hardcastle, M. J., Harris, D. E., Worrall, D. M., & Birkinshaw, M. 2004, ApJ, 612, 729
Hardcastle, M. J., Kraft, R. P., & Worrall, D. M. 2006, MNRAS, 368, L15
Hardcastle, M. J., Worrall, D. M., Birkinshaw, M., Laing, R. A., & Bridle, A. H. 2002, MNRAS, 334, 134
Hardcastle, M. J., Worrall, D. M., Kraft, R. P., Forman, C. J., & Murray, S. S. 2003, ApJ, 593, 169
Hardcastle, M. J., et al. 2007, ApJ, 670, L81
Harris, D. E., Biretta, J., Junor, W., Perlman, E. S., Sparks, W. B., & Wilson, A. S. 2003, ApJ, 586, L41
Harris, D. E., Cheung, C. C., Biretta, J., Sparks, W. B., Junor, W., Perlman, E. S., & Wilson, A. S. 2006, ApJ, 640, 211
Harris, D. E., Cheung, C. C., Stawarz, Ł., Biretta, J. A., & Perlman, E. S. 2009, ApJ, 699, 305
Harris, D. E., & Krawczynski, H. 2002, ApJ, 565, 244
Hines, D. C., Eilek, J. A., & Owen, F. N. 1989, ApJ, 347, 713
Jordán, A., et al. 2007, ApJ, 671, L117
Kataoka, J., & Stawarz, Ł. 2005, ApJ, 622, 797
Kataoka, J., Stawarz, Ł., Aharonian, F., Takahara, F., Ostrowski, M., & Edwards, P. G. 2006, ApJ, 641, 158
Kraft, R. P., Forman, C. J., Jones, C., Murray, S. S., Hardcastle, M. J., & Worrall, D. M. 2002, ApJ, 569, 54
Kraft, R. P., et al. 2000, ApJ, 531, L9
Kraft, R. P., et al. 2008, ApJ, 677, L97
Laing, R. A., & Bridle, A. H. 2002, MNRAS, 336, 328
Ma, C., et al. 1998, ApJ, 116, 516
Mainieri, V., et al. 2007, ApJS, 172, 368
Mei, S., et al. 2007, ApJ, 655, 144
Mellier, Y., & Mathez, G. 1987, A&A, 175, 1
Moretti, A., Campana, S., Lazzati, D., & Tagliaferri, G. 2003, ApJ, 588, 696
Perlman, E. S., Harris, D. E., Biretta, J., Sparks, W. B., & Macchetto, F. D. 2003, ApJ, 599, L65
Quillen, A. C., Brookes, M. H., Keene, J., Stern, D., Lawrence, C. R., & Werner, M. W. 2006, ApJ, 645, 1092
Quillen, A. C., et al. 2008, MNRAS, 384, 1469
Posson-Brown, J., Raychaudhury, S., Forman, W., Donnelly, R. H., & Jones, C. 2009, ApJ, 695, 1094
Sanders, R. H. 1983, ApJ, 266, 73
Sivakoff, G. R., et al. 2008, ApJ, 677, L27
Stawarz, Ł., Aharonian, F., Kataoka, J., Ostrowski, M., Siemiginowska, A., & Sikora, M. 2006, MNRAS, 370, 981
Tingay, S. J., & Lenc, E. 2009, AJ, 138, 808
van den Bergh, S. 1976, ApJ, 208, 673
Voss, R., et al. 2009, ApJ, 701, 471
Walker, R. C. 1997, ApJ, 488, 675
Woodley, K. A., et al. 2008, ApJ, 682, 199
Worrall, D. M., et al. 2008, ApJ, 673, L135